



# Mechanical behaviour and spatial fracture characteristics of weakly filled granite with different diameters under uniaxial loading revealed by 3D DIC and AE monitoring

Liyun Yang<sup>1</sup> · Fei Zhang<sup>1</sup> · Junxiong You<sup>1</sup> · Donghui Man<sup>2</sup> · Jun Gao<sup>3</sup> · Wei Liu<sup>1</sup>

Received: 16 August 2023 / Accepted: 8 April 2024 / Published online: 10 May 2024  
© The Author(s) 2024

## Abstract

The mechanical behaviour and failure characteristics of weakly filled granite are important factors affecting the safety and stability of rock masses. This paper presents an experimental study on uniaxial compression of granite containing both planar and circular weak filling of different diameters with the aid of three-dimensional digital image correlation (3D DIC) and acoustic emission (AE) monitoring system. The test results show the following: (1) The contact area between the planar weak filling and the bedrock is in a state of severe local deformation. The annular area of the circular weak filling in contact with the bedrock is in a severe deformation area, with detachment from the bedrock and spalling behaviour occurring. The failure modes of the specimens were summarised, and the spatial morphology of the main fracture surface was quantitatively analysed. (2) The presence of planar and circular weak filling leads to increased AE volatility. The AE hit signal is dominated by the shear signal, but the presence of circular weak filling increases the splitting signal component. (3) In the presence of circular weak filling, the energy interval of the most dominant signal is reduced, and the duration is shortened. The differences in the correlation of AE parameters are concentrated in the low-amplitude signal region. (4) Weakly filled areas will first become areas of spatiotemporal accumulation of microfracture events and will gradually spread. The accumulation and distribution characteristics of microfracture events can be used as indicators to evaluate the propensity, severity and timing of the destabilisation of rock masses containing weak filling.

**Keywords** Weakly filled granite · 3D DIC · Acoustic emission · Spatial deformation field · Failure characteristics

## Introduction

In actual construction projects and underground engineering construction activities, jointed rock masses are common construction objects, and the mechanical behaviour of rock masses is crucial to the safety and stability of rock engineering (Chen et al. 2021, 2014; Kendall 2017). However, the natural rock mass is a discontinuous material, which is rich

in various geological interfaces and impurities such as joints, laminations and pores, among which weakly filled structural surfaces are typical discontinuous layers (Sharafisafa et al. 2019; Yin et al. 2022; Huang et al. 2019; Asadizadeh et al. 2019). The non-homogeneity and discontinuity of the material composition of the weakly filled rock mass itself lead to the complexity and non-linearity of its mechanical behaviour, which brings troubles to the research related to the mechanical behaviour of weakly filled rock masses and poses a threat to the safety of related rock projects (Yu et al. 2022; Shimbo et al. 2022; Li et al. 2020; Ding et al. 2017; Tian et al. 2018), such as the rock mass with filling defects shown in Fig. 1.

A large number of studies on the mechanical behaviour of rock masses containing weak filling have been reported. The main focus has been on the geometric characteristics of weak filling, the type of filling material and the presence or absence of filling differences. In particular, experimental studies have shown that the inclination angle of weak filling

✉ Fei Zhang  
feizhang06@163.com

<sup>1</sup> School of Mechanics and Civil Engineering, China University of Mining and Technology (Beijing), Beijing 100083, China

<sup>2</sup> No.71 Engineering Company Limited, China Coal, Suzhou 234000, China

<sup>3</sup> Wuhan Guangzhou High Speed Railway Company, China National Railway Group, Wuhan 430812, China

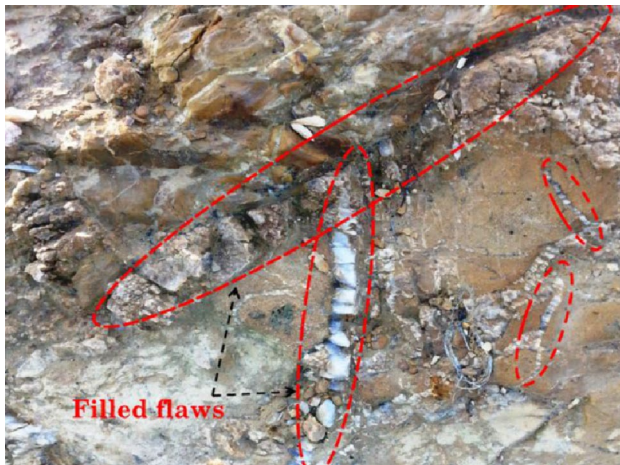


**Fig. 1** Outcrop of jointed rock mass containing filled flaws (south Sydney, M31 Highway) (Sharafisafa et al. 2019)

has a particularly significant effect on the mechanical behaviour of the rock mass (Miao et al. 2018; Srivastava and Singh 2015; Su et al. 2021; Li and Wong 2012; Han et al. 2022). Wang et al. analysed the influence of different weak filling materials on the fracture behaviour and AE characteristics of rock masses through experimental studies (Wang et al. 2022; Zhu et al. 2019; Jahanian and Sadaghiani 2015; Yu et al. 2016; Naghadehi 2015). The results are of great reference value for revealing the destabilisation mechanism of weakly filled rock masses. The presence of filling formed by artificial grouting or geological processes (Chai et al. 2020, 2022; Zhuang et al. 2014) greatly affects the mechanical properties and fracture extension behaviour of rock masses under static or dynamic loading. Liu et al. (2023a, b) and Zhang et al. (2020) analysed the factors affecting the mechanical properties using filled specimens with regular serrations, and the results showed that the peak shear strength and residual strength decreased with increasing grout water-cement ratio but increased with the increase in weak filling roughness. Specifically, the peak shear strength first decreased and then increased with increasing tilt angle, while the peak shear strength increased with increasing sawtooth height. Luo et al. (2021; 2022) conducted an experimental study on rock-like specimens with three fissures under four filling conditions: unfilled, gypsum-filled, cement-filled and resin-filled, and obtained the effects of the three fillings on the mechanical properties and failure modes of the fissured specimens. The three failure modes were summarised, and the damage mechanism of rock masses containing weak fillings was investigated.

The above studies provide a comprehensive analysis of the mechanical properties of weakly filled rock masses, and the relevant findings provide an important reference for an in-depth understanding of the destabilisation and damage

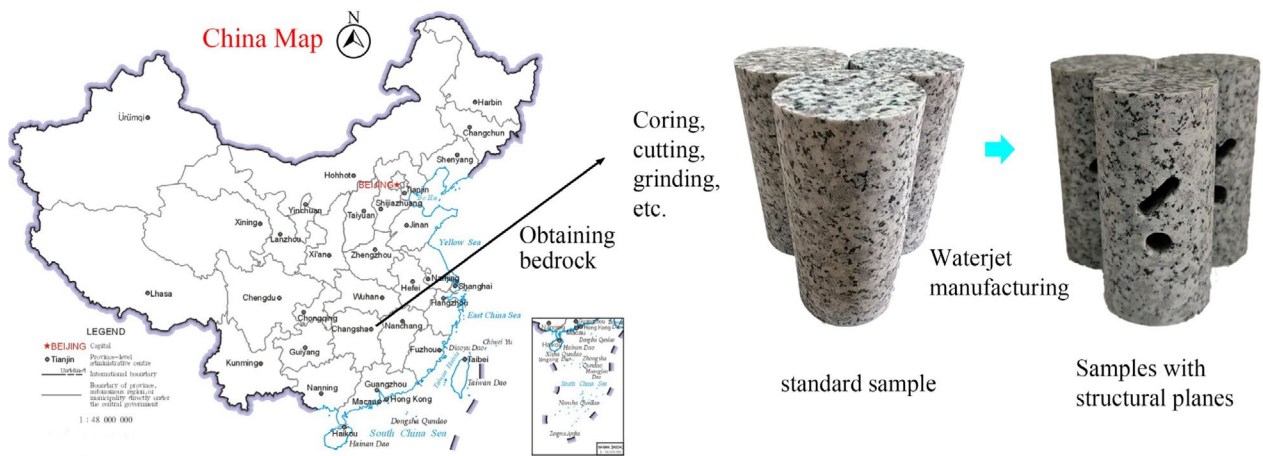
mechanisms of weakly filled rock masses and enrich the fundamental mechanical theory of non-linear rock masses. In the research process, the experimental methods are generally indoor mechanical testing experiments. Among them, AE (acoustic emission) (Aggelis et al. 2013; Chajed and Singh 2024; Zhang et al. 2015; Zhang et al. 2016; Liu et al. 2020; Ishida et al. 2017) and DIC (digital image correlation) (Sutton et al. 2009; Song et al. 2013; Dong and Pan 2017; Tang et al. 2022; Munoz et al. 2016; Zhu et al. 2022; Li et al. 2017; Zhang et al. 2018; Niu et al. 2020) are frequently used. In this paper, the mechanical properties of the weakly filled granite will be investigated simultaneously by combining the 3D DIC (three-dimensional digital image correlation) full-field-nondestructive testing technique and the AE (acoustic emission) nondestructive testing system. 3D DIC is used to obtain the evolution and distribution of the deformation field in the surface space during the loading of the specimen, while AE monitoring is used to obtain the time and frequency domain parameters of the AE and the distribution of spatial microfracture events generated during the loading of the specimen.

It is important to note that in the above reports on the mechanical properties of weakly filled rock masses, planar weak filling and circular weak filling are researched very frequently. Considering the extensive, complex and disorderly distribution of natural rock discontinuities in practical engineering, weak fillings with different geometrical characteristics are mostly endowed at the same time. Therefore, this paper aims to investigate the mechanical behaviour and AE characteristics of granite containing both planar and circular weak filling simultaneously. In this paper, compression experiments are carried out in conjunction with 3D DIC and AE, focusing on the spatial deformation field evolution and failure characteristics of the weakly filled granite containing different diameter circular inclusions. In addition, the fluctuation characteristics of AE parameters, distribution characteristics, correlation relationships and the spatial evolution and distribution characteristics of microfracture events within the specimens were comprehensively analysed using history analysis, distribution analysis, correlation analysis and spatial localisation of AE sources. The results of this paper are of certain reference value for the safe construction and stable maintenance of related weakly filled rock projects.

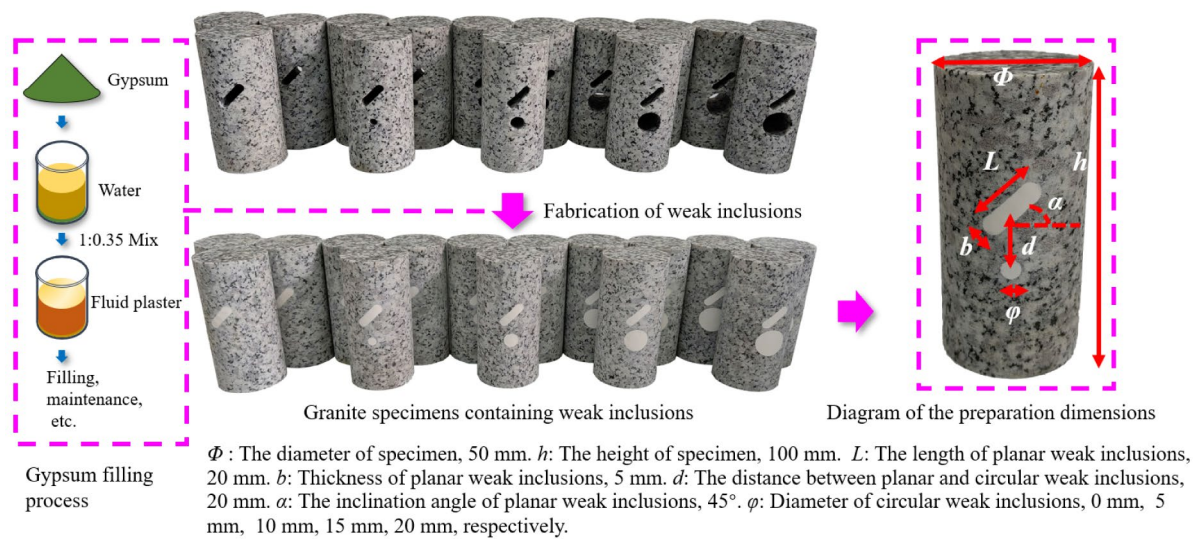
## Experimental procedures

### Specimen preparation

Granite was selected to prepare the specimen. As shown in Fig. 2, the granite specimens had an apparent size of 50 mm × 100 mm cylinders, and the processing error control



(a) Acquisition and preliminary preparation of rock samples



(b) Processing of weakly filled specimens and sample size

**Fig. 2** Sampling and processing of granite specimens with planar and circular weak filling with various diameters  $\phi$  (Note: The embedded map is from <https://bzdt.ch.mnr.gov.cn/>)

standard was following the specification (Brown 1981). The rock samples were obtained from a quarry in Yueyang City, Hunan Province, China. The quarrying area is a dorsal tectonic structure, which is subjected to horizontal compression, and some bedrock leakage is obvious. Rock samples were obtained from the quarry site by mechanical cutting and then transported to the laboratory for subsequent processing. Rock samples were removed using a coring machine to remove cylinders with a diameter of 50 mm and then cut into cylinders with a height slightly higher than 100 mm. The surface of the specimen was smoothed using a grinding machine.

Physical parameters of the rock were obtained by mechanical tests: apparent density of 2570 kg/m<sup>3</sup>, Young’s modulus

of 14.15 GPa, Poisson’s ratio of 0.24, longitudinal wave propagation velocity of 3300 m/s, uniaxial compressive strength of 101.54 MPa and tensile strength of 4.70 MPa. The purpose of this experiment was to investigate the effect of circular weak filling diameter  $\phi$  on the mechanical behaviour of rock containing the weak filling. Therefore, the specimens were designed with a planar weak filling length  $L$  of 20 mm, a thickness  $b$  of 5 mm, an inclination angle  $\alpha$  of 45° and a circular weak filling distributed below the planar weak filling with  $d=20$  mm. For the five gradients, the diameters  $\phi$  of the circular weak filling are 0 mm, 5 mm, 10 mm, 15 mm and 20 mm, respectively. Where the specimen with  $\phi=0$  mm, i.e. the case where only planar weak



filling is included. Planar and circular weak fillings run in the radial direction through the specimens.

The weak filling material is gypsum. The mechanical properties of gypsum are similar to those of weakly filled materials in natural rock, as reported in Miao et al. (2018), Janeiro and Einstein (2010) and Pan et al. (2019). Through testing, the basic physical parameters are an apparent density of  $1750 \text{ kg/m}^3$ , Young's modulus of 1.88 GPa, Poisson's ratio of 0.21, longitudinal wave propagation velocity of 2200 m/s, uniaxial compressive strength of 14.33 MPa and tensile strength 1.33 MPa. The mixing ratio of gypsum to water is 1:0.35. It is important to note that the transition area between the plaster and the rock needs to be sanded to ensure that the transition area is flat.

Processing of weakly filled samples is as follows: (1) The non-filled structural surface was drilled on the intact sample using waterjet cutting. (2) Mix gypsum and water in the ratio of 1:0.35. (3) Gypsum in a fluid state was injected into the circular and planar structural planes. (4) Maintain the plaster for 2 h and wait for the plaster to solidify. (5) Sand the specimen surface.

## Experimental system

The experimental system is shown in Fig. 3. The experimental setup consists of a loading subsystem, a 3D DIC subsystem and an AE subsystem. During the test, these systems are activated simultaneously to obtain the mechanical behaviour of the specimen and the real-time relationship between the deformation field on the surface of the specimen and the internal AE properties.

The uniaxial compressive tests were carried out at the Light Measurement Mechanics Experimental Centre of China University of Mining and Technology (Beijing).

Loading was carried out using an electric servo test system (model: E45.305, manufactured by MTS) with a maximum axial load capacity of 300 kN. During the test, axial forces were applied to both ends of the specimen at a constant vertical loading rate of 0.12 mm/min under displacement-controlled conditions until failure.

The core theory of 3D DIC is the digital image correlation method, which uses two cameras to obtain the spatial deformation field of the target object based on binocular vision theory. DIC is a particle tracking method that starts with a reference image before loading and then adds a series of photographs during loading to determine the displacement of spots in the digital image based on the correlation between them (Sutton et al. 2009; Song et al. 2013; Dong and Pan 2017). After the experiments, the images collected during the tests were computationally analysed using VIC-3D analysis software (Correlated Solutions, Inc.).

To detect the internal damage and fracture characteristics of the specimens, an AE measurement device (model: DS-2) manufactured by Soft Island Technology, Beijing, was used in the experiments. Six transducers were mounted on the surface of each specimen. Vaseline was used as a coupling agent between the specimens and the transducers. The maximum sampling capacity of the experimental system is 10 MHz. The sampling frequency was set to 3 MHz. The AE signal measured in the transducers was amplified by a preamplifier with a gain of 40 dB. In addition, a threshold of 45 dB was set for the test to avoid the possibility of electronic or environmental noise.

## Testing procedure

To perform the experiment, operate the experimental system and test the specimen according to the following steps, as

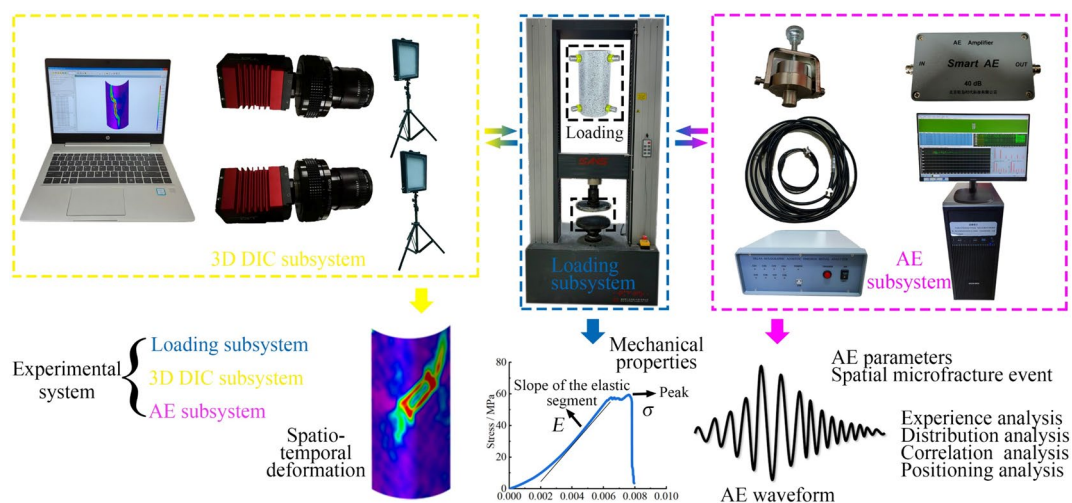


**Fig. 3** Schematic diagram of experimental system for the uniaxial compression test



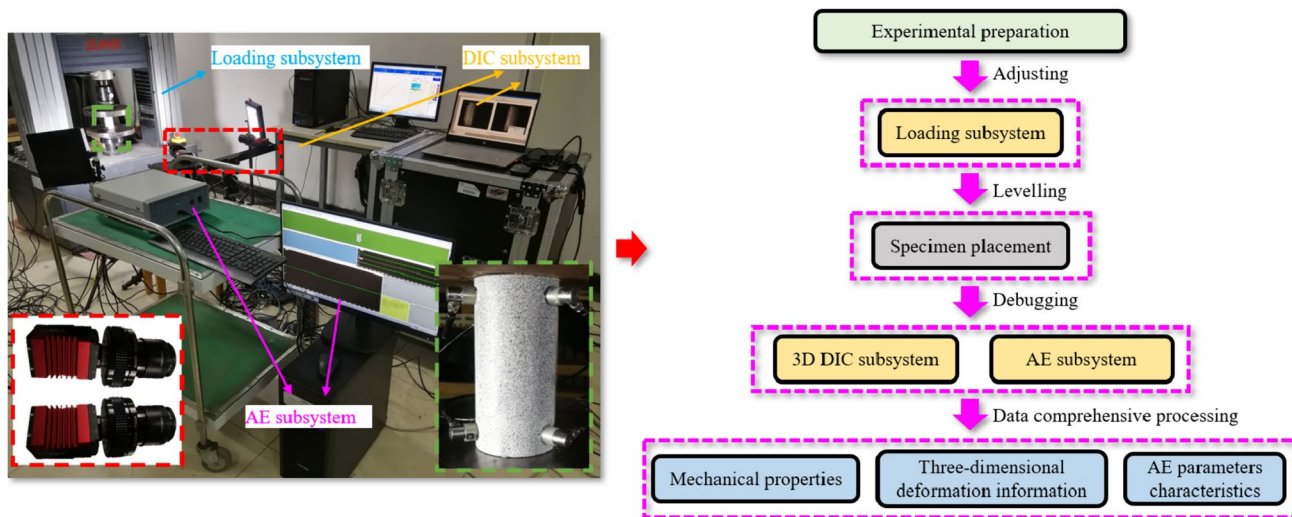


Fig. 4 Schematic diagram of equipment assembly and testing procedures

shown in the Fig. 4: (1) adjust the loading subsystem to the working state, (2) specimen placement, (3) debugging 3D DIC subsystem, (4) debugging AE subsystem, (5) testing, (6) data processing.

### Mineralogical and petrographical analyses

#### Composition determination

XRD (X-ray diffraction) tests were carried out on granite and gypsum, and the results are shown in Fig. 5. The results show that the granite is mainly composed of quartz (34.6%), potassium feldspar (8.3%), sodium feldspar (50.4%) and biotite (6.7%). The gypsum is monomeric gypsum with a

relatively simple composition, the main mineral component being  $\text{CaSO}_4 \cdot 2\text{H}_2\text{O}$  at 98.6% and anhydrite at 1.4%.

#### Microscopic morphology

The microscopic morphology of granite and gypsum was observed with the help of PLM (polarized light microscopy). The results are shown in Fig. 6. In the case of granite, combining with XRD composition determination, it can be seen that granite contains quartz, feldspar, biotite and other major mineral components. Feldspar is the most widely distributed and is shown as a large grey area in the image. Quartz content is less compared to feldspar, and the distribution area is generally loaded in the grey area, which is shown as an off-white image. In the observation field of view, there are also

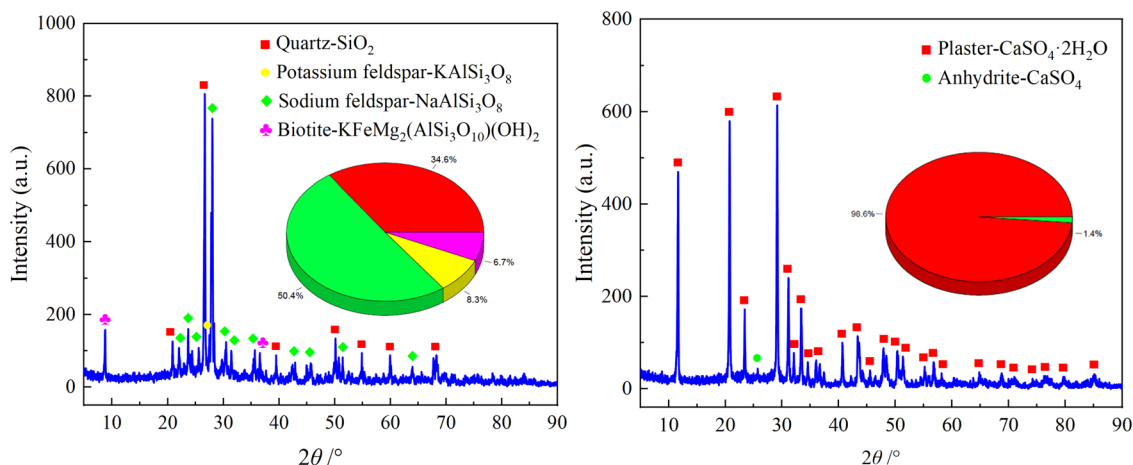
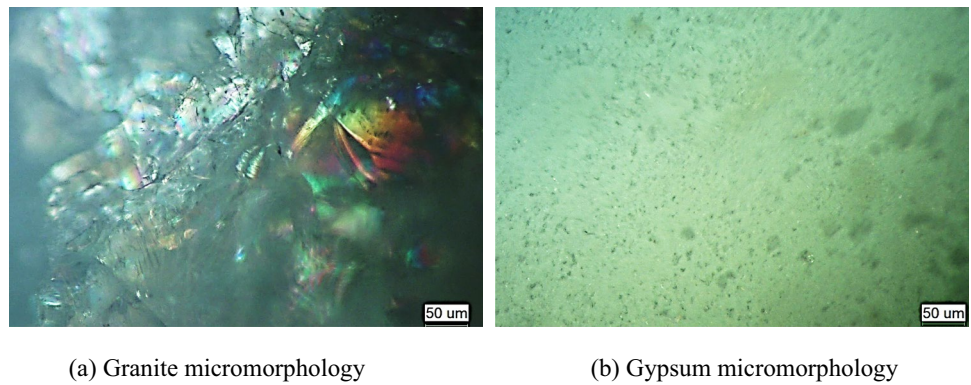


Fig. 5 XRD results of granite and gypsum. a Granite and b gypsum

**Fig. 6** PLM observation image of granite and gypsum



small black areas with scattered distribution, whose mineral composition is biotite. Biotite has an uneven surface with a black lustre and localised coloured light. For gypsum, it can be observed that the surface is a loose porous structure; the whole is relatively flat, with local microporous distribution. Since gypsum is mainly composed of calcium sulphate, the imaging characteristics under the microscope are more homogeneous.

## Mechanical characteristics

### Stress–strain relationship

As shown in Fig. 7, the stress–strain relationship and peak stress variation of specimens with different circular weak filling diameters are shown. From Fig. 7a, it can be seen that the overall stress–strain relationship shows a four-stage variation trend. Stage I is the initial compression-density stage, during which the original micro-fracture or micropores inside the specimen are closed under the compressive

load, thus showing a gradual increase in the slope of the curve. This is followed by the elastic growth phase of stage II, during which the deformation energy accumulates. As the load continues to be applied, it enters the stage III change, where the stress–strain enters a short plastic change phase, at which time the material within the specimen fails locally, damage accumulates, micro-cracks initiate and converge to form the main crack, which in turn forms the macroscopic fracture surface. Subsequently, the peak stress is reached, and the specimen enters the stage IV overall destabilisation.

The peak of the stress–strain curve is used as the static uniaxial compressive strength of the specimen to characterise the overall load-bearing capacity of the specimen. As shown in Fig. 7b, the overall load-bearing capacity of the specimen decreases with the diameter of the circular weak filling and then increases. At  $\varphi = 0$  mm, the average compressive strength of the specimen with only the circular weak filling is 76.43 MPa. The compressive strengths of the specimens are 98.88%, 62.87%, 83.41% and 94.26% of those at  $\varphi = 0$  mm for circular weak filling diameters of 5 mm, 10 mm, 15 mm and 20 mm, respectively. At  $\varphi = 5$  mm, the

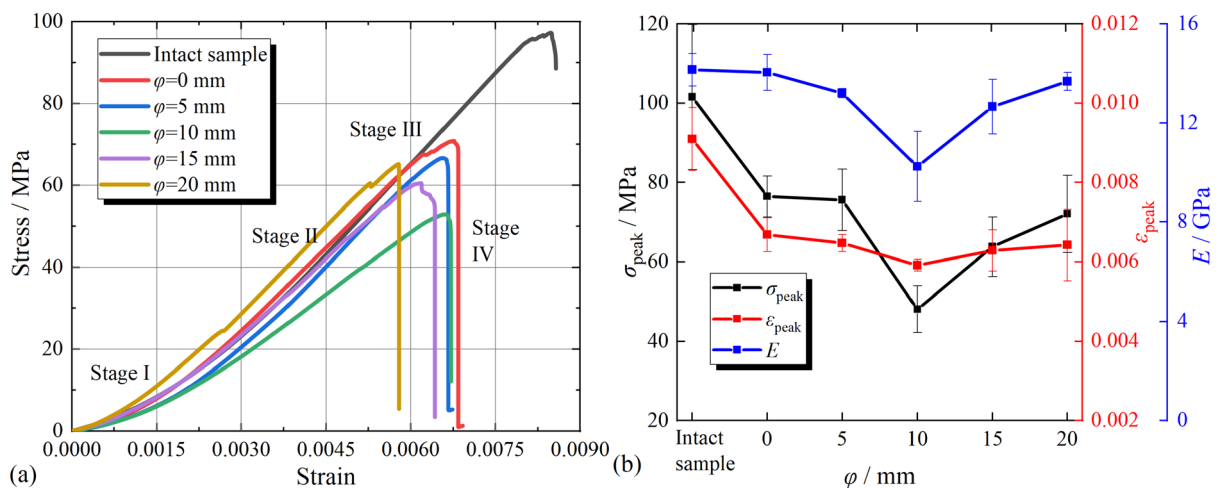


**Fig. 7** Stress–strain curves and mechanical parameter of specimen containing circular weak filling with different diameters  $\varphi$ . **a** Stress–strain curves and **b** mechanical parameter

presence of the circular weak filling increases the weak area of the specimen and therefore leads to a weakening of the overall load-bearing capacity of the specimen.  $\varphi = 10$  mm, where the overall load-bearing capacity of the specimen is the lowest, as well as the peak strain and modulus of elasticity, has the most significant weakening effect. However, the compressive strength of the specimens increased as the circular weak filling diameter increased further. This is probably because, with larger circular weak filling diameters, the circular weak filling and the planar weak filling can work together to withstand deformation and dissipate some of the deformation energy within the specimen, thus relieving the stress concentration within the specimen and thus showing an increase in the compressive strength of the specimen.

### Spatiotemporal evolution of deformation

For the sake of space, the spatiotemporal evolution of deformation of  $\varphi = 0$  mm and  $\varphi = 15$  mm specimens are taken as example. The deformation field clouds are shown in Fig. 8. In the left column, Fig. 8a, c and e shows the horizontal

strain field, vertical strain field and shear strain field of  $\varphi = 0$  mm specimen, respectively, while Fig. 8b, d and f shows the horizontal strain field, vertical strain field and shear strain field of  $\varphi = 15$  mm specimen, respectively. In the figures,  $\epsilon_{xx}$ ,  $\epsilon_{yy}$  and  $\epsilon_{xy}$  indicate the horizontal, vertical and shear strain fields, respectively, with the magnitude of the strain shown as a gradient from red to purple in the strain field.

In Fig. 8a, at the beginning of loading,  $\sigma = 0.2\sigma_{peak}$ , it can be observed that the horizontal strain field in the planar weak filling area is in an increased state. In particular, the local increase in the horizontal strain field in the red band at the contact between the upper and lower sides of the planar weak filling and the bedrock is extremely significant. This indicates that the contact area has been deformed horizontally and that there is a possibility of detachment between the planar weak filling and the bedrock. At the same time, there is a tendency for the locally increasing horizontal strain field to extend towards the bedrock at the left and right ends of the planar weak filling. As the loading continues, at  $\sigma = 0.5\sigma_{peak}$ , a red rectangle is formed around the planar weak filling in contact

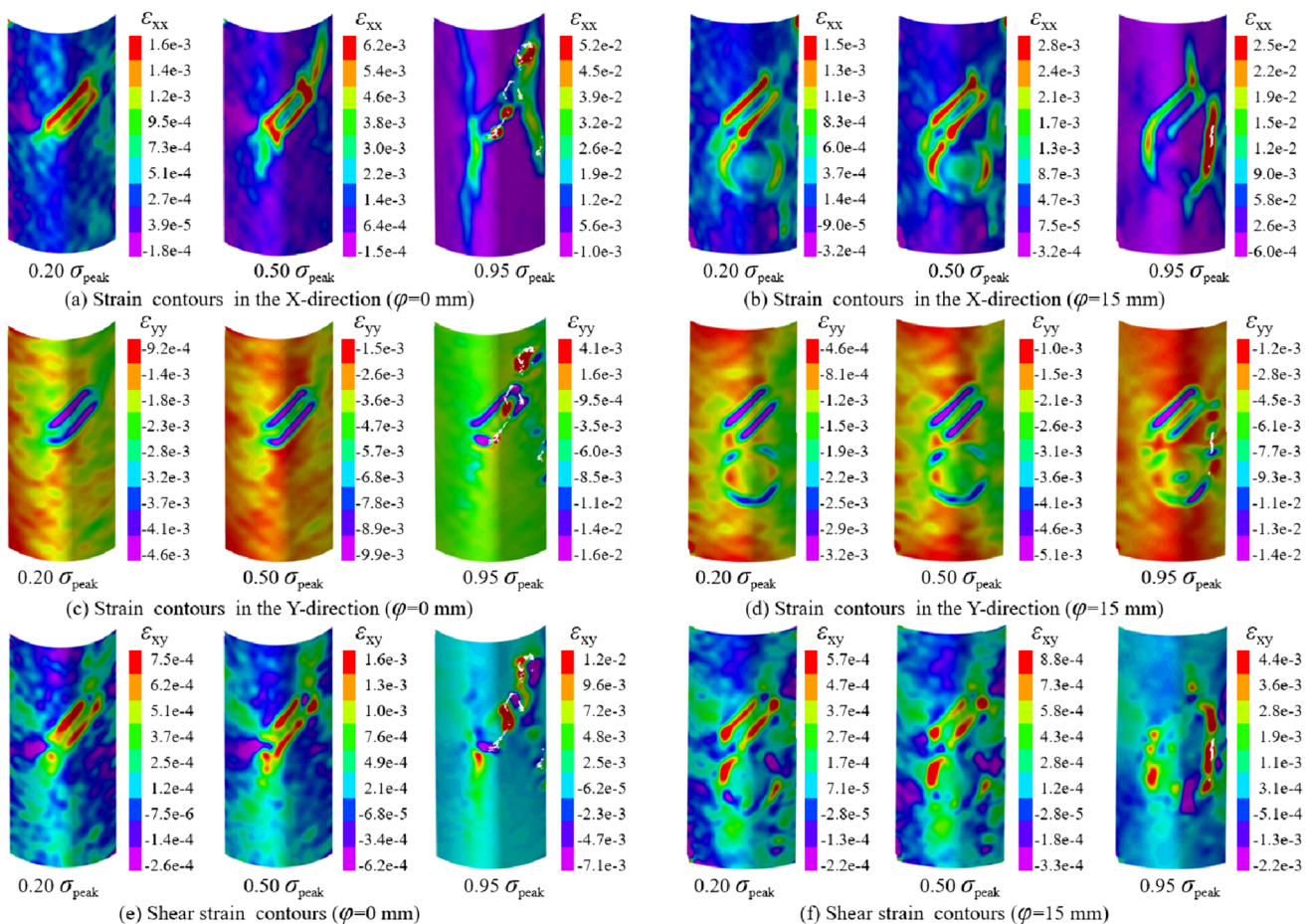


Fig. 8 Contours of the spatiotemporal evolution of the strain field



with the bedrock, and the strain continues to increase. This predicts a detachment between the planar weak filling and the bedrock due to a change in stress state during loading. At the left and right ends of the planar weak filling, the horizontal strain field increase zone extends downwards and upwards, respectively. At  $\sigma = 0.95\sigma_{\text{peak}}$ , the red rectangle of the horizontal strain field local increase zone around the planar weak filling basically disappears, which indicates that the planar weak filling has detached from the bedrock. At the same time, at the left end of the planar weak filling, an inclined zone of increased horizontal strain field is formed, indicating that the main cracking fracture propagation is occurring in this area. At the right end of the planar weak filling, the same inclined zone of horizontal strain field is present. The overall horizontal strain field increase in the specimen shows an approximate “H” shaped distribution pattern. Therefore, it can be judged that the area of the main fracture surface of the bedrock will be consistent with the local increase in the horizontal strain field when the specimen is damaged.

In Fig. 8b, the horizontal strain field is increased in the planar weak filling area at the beginning of the loading period,  $\sigma = 0.2\sigma_{\text{peak}}$ . In the circular weak filling area, the horizontal strain field is locally increased in the central part, and in the annular area where the circular weak filling is in contact with the bedrock, a circular zone of increased horizontal strain is formed, in which the left and right sides of the circular weak filling are more obvious. This indicates that the upper and lower sides of the planar weak filling are in a state of localised deformation increase in the contact area with the bedrock. At the same time, the circular weak filling is also in a state of increased local deformation at the contact with the bedrock, and there is a risk of detachment from the bedrock in these areas. The overall profile of these areas forms a “ $\sigma$ ”-shaped distribution pattern. As the loading continues, the horizontal strain increases further in the above-mentioned areas of increased local deformation at  $\sigma = 0.5\sigma_{\text{peak}}$ . This is particularly evident at the left and right ends of the planar weak filling and tends to extend downwards and upwards, respectively. This means that not only does the planar weak filling detach from the bedrock, but the circular weak filling also detaches. At  $\sigma = 0.95\sigma_{\text{peak}}$ , the horizontal strain field is in the zone of increased banding at the planar weak filling and extends downwards and upwards at the left and right ends of the planar weak filling, respectively. This predicts that when the specimen is damaged, the crack will extend downwards at the left end of the planar weak filling and upwards at the right end. Furthermore, the horizontal strain field is also at a local increase to the left and right of the circular weak filling, which predicts that crack propagation will also occur in this region.

From Fig. 8c–f, it can be seen that the spatial evolution and distribution characteristics of the vertical and shear deformation fields are affected by the weak filling. The

main feature is that when the diameter of the circular weak filling increases, the local deformation region evolves into a ring-shaped region where the circular weak filling is in contact with the bedrock. This suggests that the location of macroscopic failure propagation of the specimen has been changed, which will lead to the variability of the overall damage pattern of the specimen.

The horizontal strain field, vertical strain field and shear strain field of  $\varphi = 0$  mm and  $\varphi = 15$  mm specimens can be compared and analysed above, and it can be seen that the spatial evolution of deformation mainly shows the following characteristics: (1) The contact area between the planar weak filling and bedrock is in a state of severe local deformation, and it extends towards the bedrock at both ends as the loading continues. The presence of circular weak filling does not significantly change the local deformation behaviour of the planar weak filling. (2) The annular area where the circular weak filling is in contact with the bedrock is in severe horizontal deformation on the left and right side, severe vertical deformation on the upper and lower side and severe shear deformation on the upper left, lower right, lower left and upper right side.

### Failure characteristics

The failure characteristics of weakly filled rock masses are useful references for the stability control analysis of engineering rock masses. Figure. 9 shows the failure mode and crack distribution of the specimen.

As can be seen from the figure, the final mode of  $\varphi = 0$  mm specimen is an integral shear failure. The main crack is a shear crack, which originates from the planar weak filling and propagates downwards and upwards at the left and right ends of the planar weak filling, respectively, and extends through to the end of the specimen. The secondary cracking starts at the end of the planar weak filling and extends into the bedrock. The planar weak filling detached from the bedrock and the planar weak fill itself is partially spalled.  $\varphi = 5$  mm specimens are finally damaged in integral shear. The main crack initiation and extension behaviour is similar to that of the  $\varphi = 0$  mm specimen, i.e. it originates in the planar weak filling and propagates downwards and upwards at the left and right ends of the planar weak filling, respectively, extending through to the end of the specimen. It is noteworthy that the secondary crack at the left end of the planar weak filling is guided by the circular weak filling as it extends into the bedrock below.  $\varphi = 10$  mm specimen was ultimately damaged in integral shear, with similar failure characteristics to  $\varphi = 5$  mm specimen.  $\varphi = 15$  mm specimen ultimately failed in integral shear. The main crack was a mixed shearing and splitting crack, which originates from the planar weak filling and propagates downwards and upwards at the left and right ends of the planar weak filling,

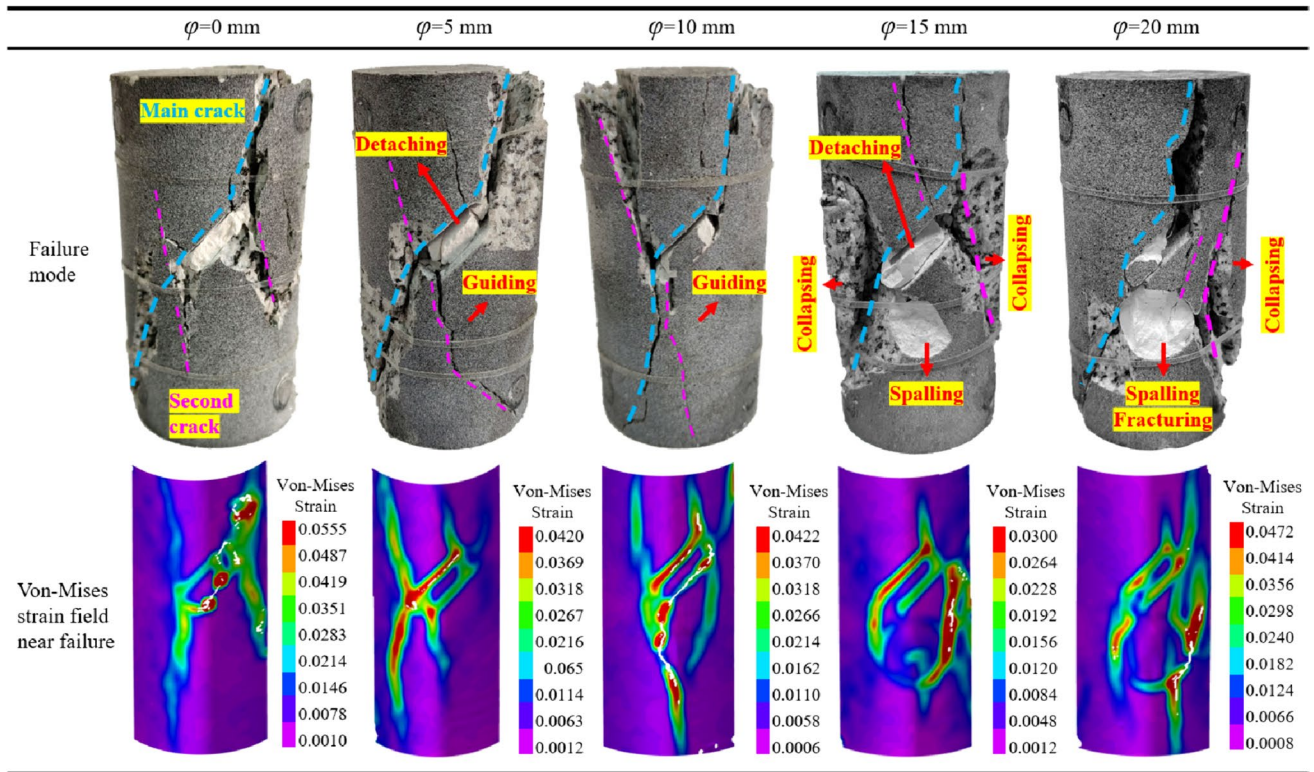


**Fig. 9** Schematic diagram of the final failure mode and crack distribution of the specimens containing different diameter circular inclusions

respectively, and extends through to the end of the specimen. More severe spalling of the bedrock occurs at the left and right ends of the planar weak filling. The planar weak filling was detached and crumbled. The final failure mode of the  $\varphi = 20$  mm specimen is an integral shear failure. The failure characteristics are similar to those of the  $\varphi = 15$  mm specimen.

The failure characteristics of the specimens in Fig. 9 and the strain field distribution characteristics in Fig. 8 show that for specimens without circular weak filling, i.e. specimens with only planar weak filling, the failure mode is an integral shear failure. However, the presence of the circular weak fill leads to different failure characteristics of the bedrock around the circular weak filling, mainly in that the propagation of the secondary cracks at the left end of the planar weak filling was guided by the circular weak filling. When the diameter of the circular weak filling increases to 15 mm and 20 mm, a more obvious collapse occurs on the left and right sides of the circular weak filling. This is probably because the bedrock in the path of sub-crack propagation has been occupied by the circular weak filling, and the elastic energy released by the destabilisation of the rock mass has not been released in the form of crack propagation, thus outwardly manifesting itself as the occurrence of the localised crumbling of the bedrock. In addition, the planar weak filling itself is detaching from the bedrock, and spalling occurs

to some extent. However, circular weak fillings do not detach themselves from the bedrock and spall to some extent until they are larger in diameter.

### Fractal characteristics of fracture surface

In the process of macroscopic failure of specimens subjected to static loading, the fracture surface is the dominant factor influencing the final macroscopic failure characteristics. Some studies have shown that the geometry of the fracture surface has fractal characteristics (Zhang and Zhao 2013; Nasseri et al. 2009; Zhou and Xie 2008). Therefore, based on the fractal theory and with the help of 3D laser scanning technology, the fine fractal characteristics of the fracture surface are analysed. Specifically for the calculation of the fractal dimension of the rock fracture surface, the 3D cube coverage method is widely used, convenient and accurate (Zhou and Xie 2008; Ai et al. 2014).

The calculation process is shown in Fig. 10. Three-dimensional laser scanning was used to obtain the spatial morphology of the fracture surface and digitise it, extract the spatial coordinates of the fracture surface ( $x, y, z$ ) from the point cloud data and carry out fractal calculations on the spatial coordinates to obtain the fractal dimension of the fracture surface.

The specific calculation principle is as follows: on the plane  $XOY$ , a square grid with side length  $\delta$  is taken

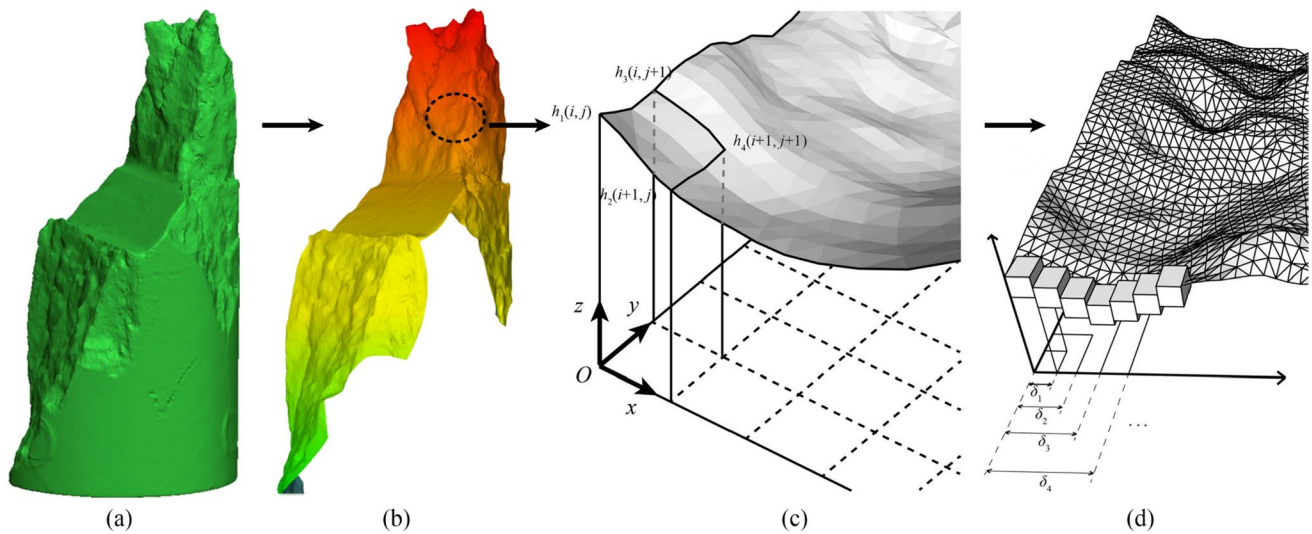


**Fig. 10** Flowchart of 3D spatial topography data morphology of fracture surface and fractal calculation by cubic cover method. **a** 3D morphology of the fractured rock mass; **b** 3D spatial point cloud data materialisation of the fractured surface; **c** projected local schematic

of the digitised fractured surface; **d** local schematic of the fractured surface covered by a cube with edge length  $\delta$  (Zhou and Xie 2008; Ai et al. 2014; Yin et al. 2019)

randomly, and the 4 heights  $h_1(i, j)$ ,  $h_2(i + 1, j)$ ,  $h_3(i, j + 1)$  and  $h_4(i + 1, j + 1)$  correspond to the 4 corners of this square grid (where  $i \geq 1, j \leq n - 1$ , and  $n$  is the number of grids needed to cover the plane  $XOY$ ).

Cover the fracture surface with a square grid with side length  $\delta$ . Calculate the number of cubes in the coverage area  $\delta \times \delta$ , i.e. the number of cubes covering the fracture surface in the  $(i, j)$  grid is  $N_{ij}$  (Zhou and Xie 2008; Ai et al. 2014; Yin et al. 2019):

$$N_{ij} = \text{INT} \left\{ \frac{1}{\delta} \left[ \max(h_1(i, j), h_2(i + 1, j), h_3(i, j + 1), h_4(i + 1, j + 1)) - \min(h_1(i, j), h_2(i + 1, j), h_3(i, j + 1), h_4(i + 1, j + 1))) \right] + 1 \right\} \tag{1}$$

where INT is the rounding function.

The total number of cubes  $N$  required to cover the entire fracture surface is as follows:

$$N(\delta) = \sum_{i,j=1}^{n-1} N_{ij} \tag{2}$$

Change the scale of  $\delta$  to cover it again and then calculate the total number of cubes needed to cover the entire fracture surface. The fracture surface has fractal features as the following relationship between the total number of cubes  $N(\delta)$  and  $\delta$ :

$$N(\delta) \sim \delta^{-D} \tag{3}$$

where  $D$  is the self-similar fractal dimension of the fracture surface.

The spatial coordinates  $(x, y, z)$  extracted from the point cloud data of the fracture surface are subjected to the above calculation, and the results are logarithmically transformed; a series of data points  $\ln N(\delta)$  and  $\ln \delta$  can be obtained; fitting

$\ln N(\delta)$  and  $\ln \delta$ , there is a linear functional relationship between the two, in which the slope is the fractal dimension  $D$ . The mentioned mathematical relationship is as follows:

$$D = -\lim_{\delta \rightarrow 0} \frac{\ln N_\delta(\Sigma)}{\ln \delta} \tag{4}$$

where the fractal dimension  $D$  is generally between 2.0 and 3.0. In general, when the observation scale  $\delta > 1.25$  mm, the fractal dimension  $D \rightarrow 2.0$ , i.e. the fractal characteristic tends to disappear, which can be regarded as the fracture surface is extremely smooth; when the observation scale  $\delta < 1.25$  mm, the fractal characteristic appears on the fracture surface, which can be regarded as the irregularity of the fracture surface, and the roughness increases.

Using the above method, the spatial morphology of the main fracture surface of the specimen with  $\varphi = 0$  mm and  $\varphi = 15$  mm specimens is shown in Fig. 11.

From the spatial morphology of the main fracture surface of the specimen in Fig. 11, it can be seen that for the



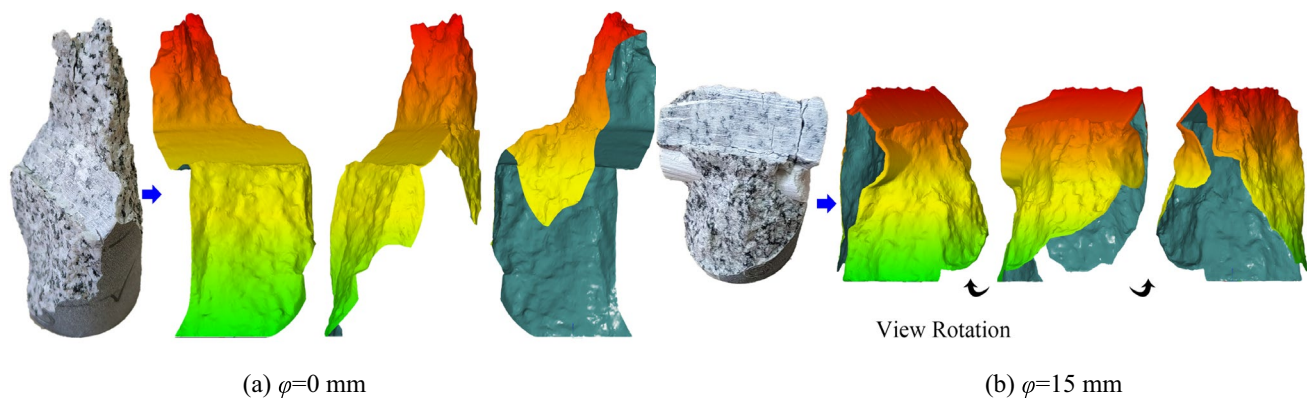


Fig. 11 Schematic of the spatial morphology of the fracture surface of the specimen

$\varphi = 0$  mm specimen, the main fracture surface extends to the upper bedrock at the upper end of the planar weak filling; the main fracture surface extends to the lower bedrock at the lower end of the planar weak filling. The main body of bedrock has an overall peak-like morphology. The surface of the fracture surface is uneven, and the overall extension trend is undulating in three-dimensional space. The bedrock is locally fractured but not dislodged. In the contact area between the weak filling and bedrock, gypsum powder was left behind, showing obvious friction traces, which confirmed that there was friction and slip movement between the weak filling and bedrock in the process of loading the specimen as a whole, and the weak filling thus detached from the bedrock.

For the  $\varphi = 15$  mm specimen, above the circular weak filling, the main fracture surface does not continue upwards because the bedrock is fractured. This may be due to the presence of transverse tensile stresses in the bedrock above the circular weak filling; the bedrock is therefore susceptible to fracture failure due to the tensile stresses reaching their limit states. Combined with the final failure result of

the specimens, it can be seen that the bedrock at this location is “flaked” and large chunks of the bedrock “crumbled.” Below the planar weak filling, the fracture surface extends downward with an undulating surface. It should be noted that the circular weak filling itself does not show significant fracturing. The extension of the fracture surface in space mainly develops in the bedrock on both sides of the circular weak filling.

Comparing the above analyses, it can be seen that the increase of the diameter of the weak filling obviously affects the spatial morphology of the main fracture surface of the specimen. To quantitatively evaluate the surface undulation characteristics of the main fracture surface, the results of fractal dimension calculation are shown in Fig. 12.

The size of the fractal dimension of the fracture surface is different for different specimens: for  $\varphi = 0$  mm and  $\varphi = 15$  mm specimens,  $D$  is 2.5114 and 2.5215, respectively. Therefore, it can be considered that the fractal dimension of the main fracture surface of the specimen is affected to a certain extent when the diameter of circular weak filling is different. In combination with other reports (Yin et al. 2019),

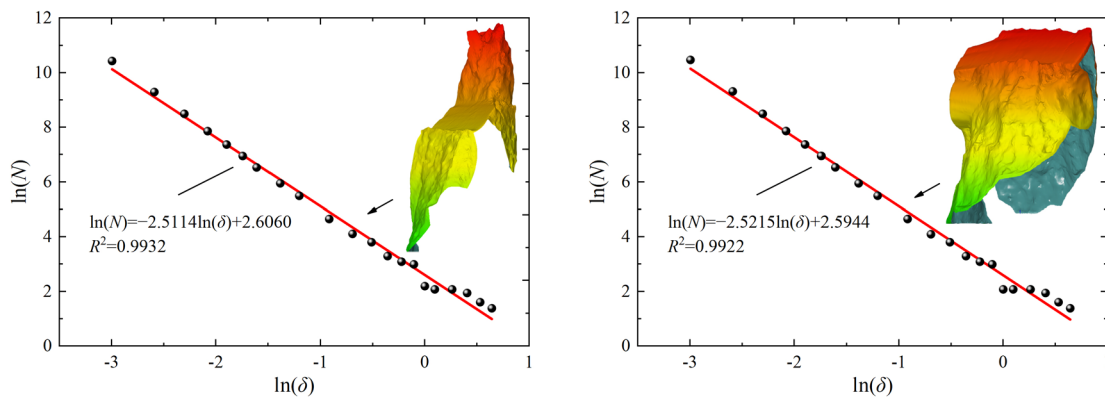


Fig. 12 Calculation results of fractal dimension of the main fracture surface of the specimen

the magnitude of this variability is generally small, while the specific working conditions in which the rock is located and the type of rock are closely related. Therefore, the reason for the small variability of results in this experiment is most likely that the presence of granite mineral grains can lead to a random nature of microcrack propagation.

Combined with Yin et al.'s report (Yin et al. 2019; Carpinteri et al. 1999; Ma et al. 2019; Zhang and Zhao 2013), it can be seen that the fracture surface morphology characteristics of the rock mass are affected by the distribution of mineral particles, strain rate, temperature and other factors. For example, in Yin's report, the fractal dimension is 2.21/2.42/2.46 for cyclic loading 1/10/20 times at 400 °C. However, the results of the present experiment show that the fractal dimension of the fracture surface of the  $\varphi=0$  mm and  $\varphi=15$  mm specimens are 2.5114 and 2.5215, respectively. The reason for the relatively small difference is that although the presence of the weak filling affects the specimen's failure mode, however, the effect on the fractal undulation characteristics of the fracture surface is small because in this experiment, the weak filling did not change the mineral composition of the granite bedrock at the time of fracture surface formation and only had a macroscopic effect on the final failure mode. Therefore, the difference in the fractal dimension calculation results is only in the percentile.

Although the presence of circular weak filling causes the extension of the main fracture surface in space to be affected,

the difference in fine morphology is not fully revealed. This provides an idea for quantitative evaluation of the fine-scale features of the fracture surface, which is still of some reference significance.

### Mineralogical and petrographical characteristics

Taking  $\varphi=0$  mm and  $\varphi=15$  mm specimens as examples, XRD and PLM tests were carried out on the granite and gypsum of the post-damage specimens to analyse the composition and micro-morphological features of the granite and gypsum of the specimens with different mechanical properties. The following Fig. 13a and b shows the XRD test results of granite of  $\varphi=0$  mm and  $\varphi=15$  mm specimens, respectively; c and d show the XRD test results of gypsum of  $\varphi=0$  mm and  $\varphi=15$  mm specimens, respectively.

From the results, it can be seen that the mineral compositions of granite in different specimens are basically the same, mainly containing quartz, sodium feldspar, potassium feldspar and biotite. In terms of composition, for  $\varphi=0$  mm, quartz is 62.4%, sodium feldspar 23.1%, potassium feldspar 5.6% and biotite 8.9% and for  $\varphi=15$  mm, quartz is 35.4%, sodium feldspar 33.8.1%, potassium feldspar 15.7% and biotite 15.1%. The composition of gypsum minerals in the different specimens is mainly calcium sulphate, and the percentage of content is very high, above 99.0%. No anhydrite was detected in  $\varphi=0$  mm specimen.

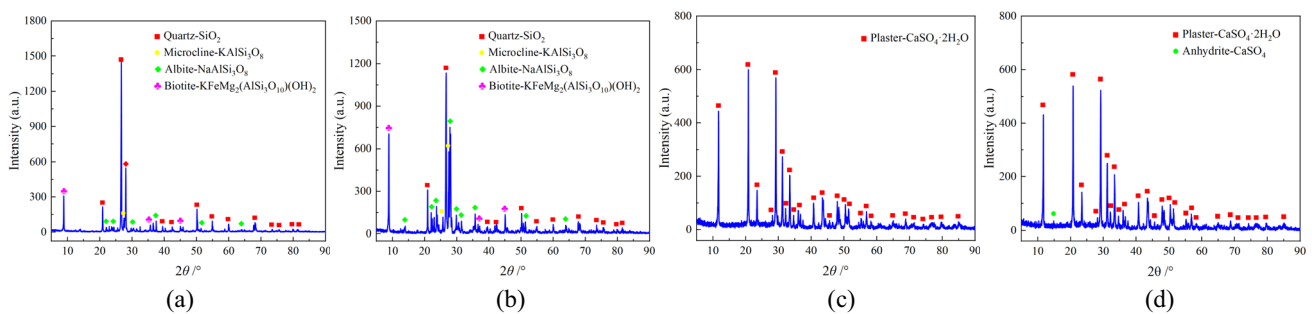


**Fig. 13** XRD results for granite and gypsum. **a** Granite of  $\varphi=0$  mm specimen, **b** granite of  $\varphi=15$  mm specimen, **c** gypsum of  $\varphi=0$  mm specimen, **d** gypsum of  $\varphi=15$  mm specimen

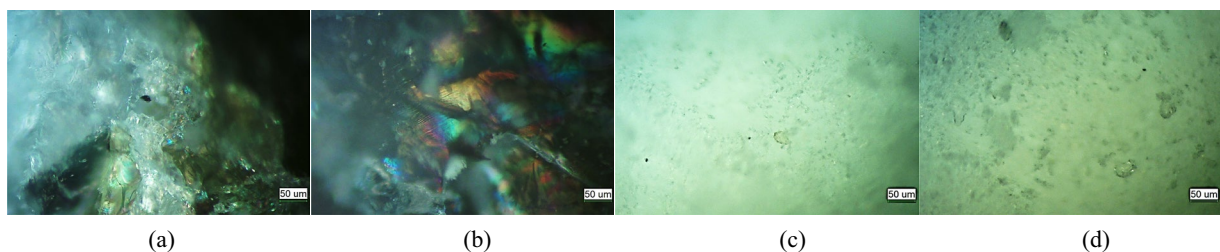


**Fig. 14** PLM results for granite and gypsum. **a** Granite of  $\varphi=0$  mm specimen, **b** granite of  $\varphi=15$  mm specimen, **c** gypsum of  $\varphi=0$  mm specimen, **d** gypsum of  $\varphi=15$  mm specimen

The PLM identification results of granite and gypsum are shown in Fig. 14. As can be seen from Fig. 14a and b, the microforms all have typical petrographic features of granite minerals. Quartz, feldspar and biotite are distributed in mutual mosaic. Locally, the mineral grains are loosely distributed, and microcracks are occasionally distributed. This may be due to the change of force chain distribution and interaction relationship between mineral particles in the microscopic scale during the loading process of the specimen. From Fig. 14c and d, it can be seen that the micro-morphological characteristics of gypsum did not show significant variability.

Combining the XRD and PLM test results, it is reasonable that for granite and gypsum with specimens having different mechanical properties, the mineral compositions remain basically the same. This is because the reason for the change of different mechanical properties is that the specimens contain weak fillings with different diameters of circular weak filling. The presence of weak filling leads to a change in the stress transfer path when the specimen is subjected to loading, thus revealing a difference in the macroscopic mechanical properties. Meanwhile, the micro-morphological characteristics of granite and gypsum are generally in high agreement. Succinctly, the presence of weak filling leads to changes in the macroscopic mechanical properties of the specimens but does not significantly affect the mineralogical and petrological characteristics. This can be intuitively interpreted to mean that the mechanical properties of weakly filled granites are externally “macrostructure” due to the presence of weak fillings, rather than a change in the material properties of the rock or filler itself.

### Characteristics of AE parameters

The main parameters of the AE waveform are ringing count, hit count, energy, amplitude, duration, etc. Its signal simplification waveform parameters are defined as shown in Fig. 15.

The AE signals with a higher AF (average frequency) value and lower RA (rise angle) value mean tensile cracks and the inverse means shear cracks. History analysis, distribution analysis, correlation analysis and localisation analysis of AE parameters can be carried out to evaluate the AE characteristics of the sample as its mechanical behaviour changes.

### Characteristics of AE parameters

The fluctuation histories of AE counts and cumulative AE counts were analysed. Figure. 16 shows the trend of stress history; AE counts history and cumulative AE counts history of  $\varphi=0$  mm and  $\varphi=15$  mm specimens.

As can be seen from Fig. 16a, the AE counts fluctuate at a low level at the beginning of the loading period, when the original microfractures and micropores inside the specimen are closed under the action of the compression load. At  $t=400$  s later, the AE counts start to grow at a high level, and correspondingly, the cumulative AE counts also start to grow rapidly. Of particular importance is that during the spatiotemporal evolution of the specimen deformation field, at this stage, the local increase zone of the deformation field in the planar weak filling area starts to extend below and above the bedrock at the left end and right end portions, respectively. This implies the convergence of micro-cracks and the formation of macro-cracks in the specimen and the

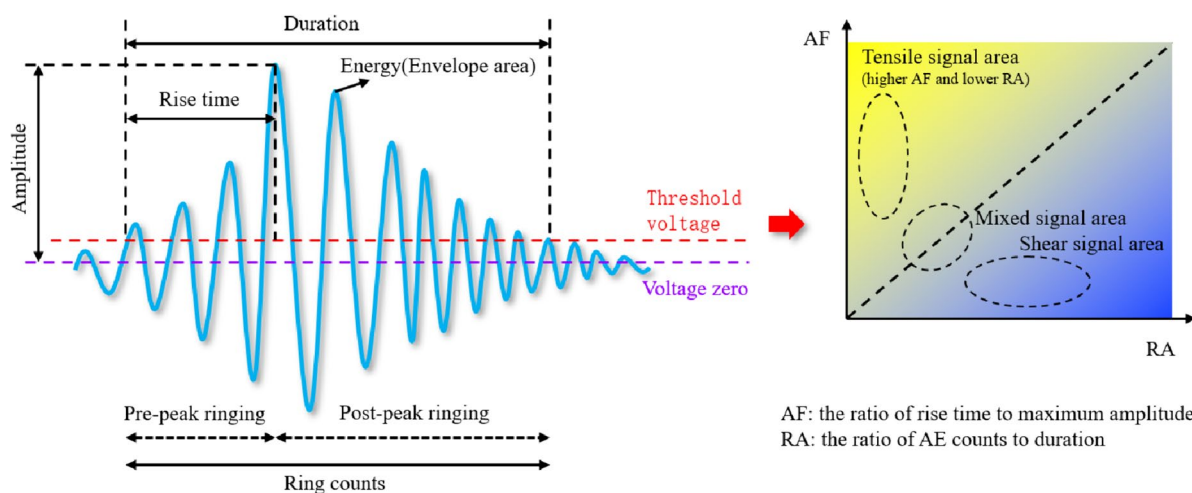


**Fig. 15** Definition of simplified waveform parameters for AE signals and diagrams of crack classification based on the distribution of RA-AF values (Shen 2015; Li et al. 2023)



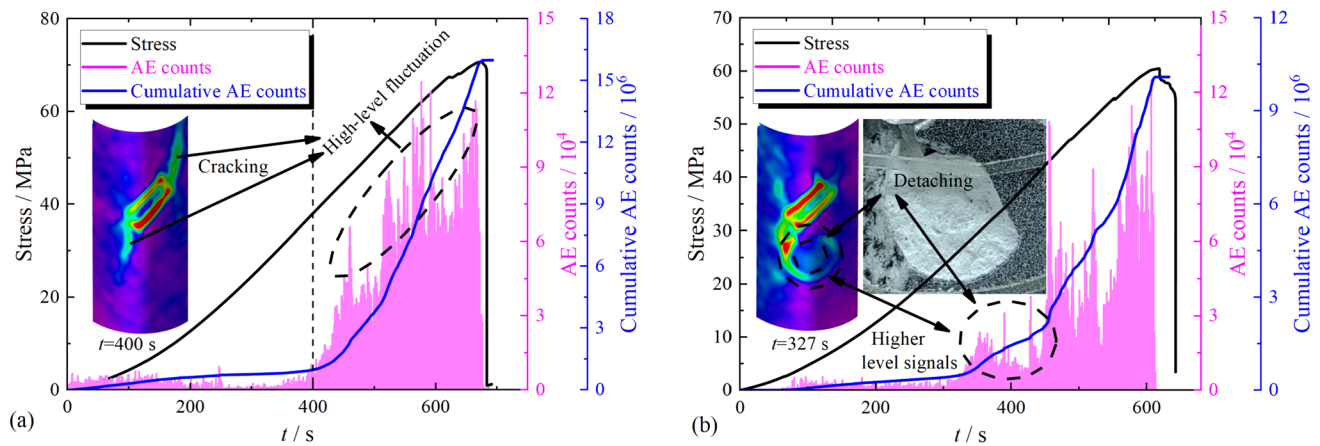


**Fig. 16** AE counts, cumulative AE counts fluctuation history: **a**  $\varphi=0$  mm and **b**  $\varphi=15$  mm

imminent failure of the specimen. After  $t=600$  s, the stress changes show plastic characteristics, indicating that the specimen undergoes plastic damage and starts to enter the plastic-yielding stage. The AE counts continue to increase at a high level. This means that the local failure behaviour of the material within the specimen continues to occur, and the main fracture surface is forming. Corresponding to the deformation field in Fig. 8a adjacent to the peak stress, it can be seen that at this point, a localised large deformation zone profile forms and the macroscopic main crack propagates. As the loading continues and the stress grows to the peak stress, the specimen fails as a whole, and the level of AE counts fluctuations falls rapidly and tends to disappear, implying the completion of the whole loading process of the specimen.

The stress, AE counts and cumulative AE counts are shown in Fig. 16b for the circular weak filling specimen with diameter  $\varphi=15$  mm. As can be seen from the figure, the AE counts fluctuate at a low level at the beginning of the loading process, and after  $t=300$  s, there is a brief increase in the AE counts at a high level. Combined with the evolution of the spatial deformation field of the specimen, it can be seen that at this stage, the upper and lower sides of the planar weak filling are in a state of increased local deformation in contact with the bedrock, and at the same time, the circular weak filling is also in a state of increased local deformation in contact with the bedrock. The occurrence of local deformation in these areas is inevitably accompanied by frequent AE from local material failure, resulting in a transient high-level increase in AE counts. It should be noted that for specimen with only planar weak filling ( $\varphi=0$  mm), there is no transient high-level increase in AE counts. It can be inferred that the presence of circular weak filling was the cause. Immediately, after  $t=400$  s, the AE count soon enters a high-level fluctuation phase, at which time localised detachment and spalling of the planar weak filling and

circular weak filling occurs, and the main crack originates in the planar weak filling and extends towards the bedrock at the left end and right end. At around  $t=600$  s, the stress growth is about to reach its peak, and the specimen is about to fail; the AE activity is at a high level of fluctuation, and the cumulative count is increasing rapidly. Subsequently, the specimen undergoes overall destabilisation.

### AE waveform characteristics

The AE signal is mainly in the form of waves, and the waveform characteristics are evaluated in terms of the distribution dynamics of the angle of rise (RA) and the average frequency (AF) of the AE hit signal; RA is defined as the ratio of rise time to maximum amplitude, and AF is defined as the ratio of AE counts to duration. As shown in Fig. 15 and the results in Fig. 17, the waveform of tensile crack mainly propagates in the form of long longitudinal wave, which leads to the low RA value. The waveform of shear crack mainly propagates in the form of shear wave, resulting in the low AF value. Hence, the points in the tensile signal area have a small RA value and large AF value, and the points in the shear signal area have a small AF value and large RA value. In addition, RA and AF value of the points near the critical line are approximately similar, which accords with the characteristics of mixed crack. Here, the unit of RA is in ms/V, and the unit of AF is in kHz. The RA/AF distributions for  $\varphi=0$  mm and  $\varphi=15$  mm specimens are shown in Fig. 17.

As can be seen from Fig. 17a, the hit signal is mainly distributed in the shear signal region. The distribution range of RA is (0,200) ms/V. The distribution range of AF is (0,600) kHz and is mainly concentrated in the range of 0–300 kHz. The larger the RA, the smaller the distribution range of AF and the lower the upper limit of the interval. The upper interval of the AF distribution forms

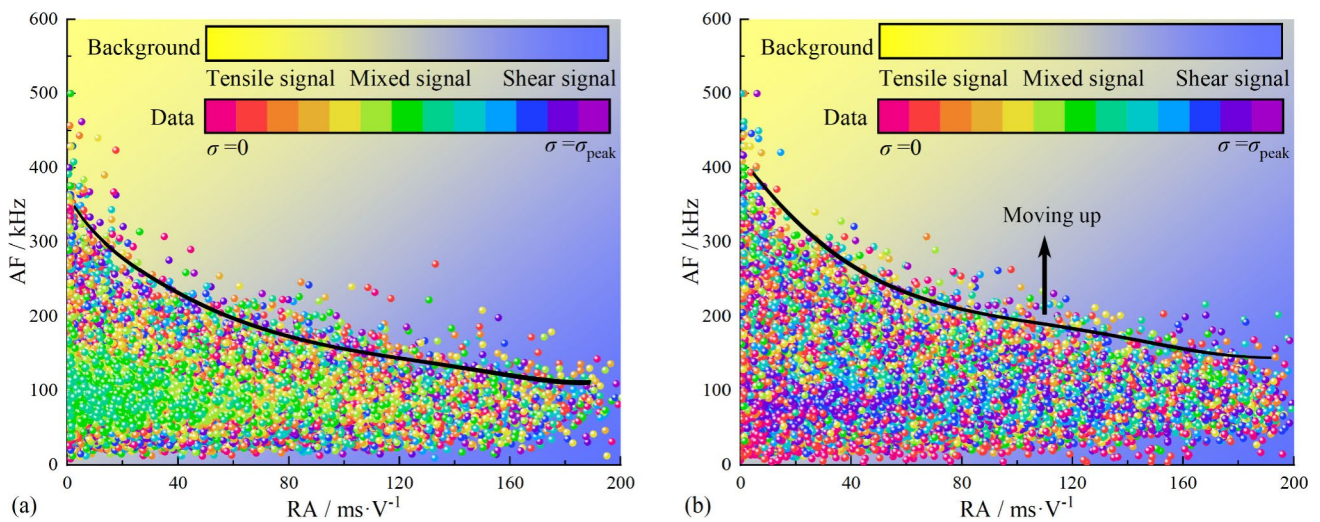


**Fig. 17** Distribution of mean frequency and angle of rise of AE signal: **a**  $\varphi=0$  mm and **b**  $\varphi=15$  mm

a downward curved envelope, as shown by the black line in the figure. The appearance of hit signals in the figure is distributed throughout the loading process, and it can be observed that there are more hit signals in yellow, which indicates that more shear signals were generated during the pre-loading period, which may be related to the shear deformation generated during the frictional slip between the planar face weak filling and the bedrock. Combined with the failure pattern of the specimen in Fig. 9, it can be seen that shear failure occurred in the specimen as a whole therefore, the waveform characteristics of the hit signal are mainly distributed in the shear signal area.

Figure 17b shows the distribution of RA/AF for the  $\varphi=15$  mm specimen. As can be seen from the figure, the distribution of the hit signal is mainly in the shear signal region. As the RA varies from small to large, the distribution of AF gradually transitions from (0,600) to (0,200) kHz. The dense area in the upper zone of the AF distribution forms a downward curved envelope, as shown by the black line in the figure. However, this envelope shifts upwards relative to the envelope in Fig. 17a, which indicates that the hit signal has increased with high AF values. Combined with the failure pattern of the specimen in Fig. 9, it is clear that the main crack pattern above the right end of the planar weak filling is a splitting crack, with more severe collapsing occurring in the bedrock to the left of the left end of the planar weak filling and to the right of the right end of the planar weak filling, and spalling of the circular weak filling itself. The initiation of splitting cracks, the occurrence of collapsing, the spalling of weak filling itself and the local failure of the material all produce elastic waves dominated by tensile longitudinal waves, which lead to an increase in AF in the hit signal.

### Distribution characteristics AE parameters

The distribution characteristics of the recorded AE parameters characterise the activity of the source. The distribution characteristics of the amplitude, energy and duration of the AE parameters are analysed. The statistical results are shown in Fig. 18.

As can be seen from Fig. 18a, for the  $\varphi=0$  mm specimen, the largest proportion of the hit signal amplitude distribution was in the interval (54,55) dB, at 13.96%, and the proportion gradually decreased with higher amplitude. The mean value of the hit signal amplitude is 60.03 dB, with a standard deviation of 5.74 dB. Figure. 18b shows that for  $\varphi=15$  mm specimen, the largest proportion of the hit signal amplitude distribution was still in the interval (54,55) dB, at 14.04%, with the proportion decreasing with higher amplitude. The mean value of the hit signal amplitude was 59.97 dB with a standard deviation of 5.64 dB. The comparison shows that there is no significant difference in the amplitude distribution characteristics of the hit signals. This is because the overall failure mode of the specimen is a shear failure, and the local source energy release during the local failure of the internal material is mainly carried by the generation of low-amplitude shear waves, so the AE amplitude distribution is still dominated by low-amplitude signals.

As can be seen from Fig. 18c, for  $\varphi=0$  mm specimen, the hit signal energy distribution in the interval (2,3) mV\*ms has the largest percentage of 12.32%, and the higher the energy, the percentage gradually decreases. The mean value of the hit signal energy is 19.11 mV\*ms, and the standard deviation is 83.66 mV\*ms. Figure. 18d shows that for  $\varphi=15$  mm specimen, the largest proportion of the hit signal energy distribution was in the interval (1,2) mV\*ms,

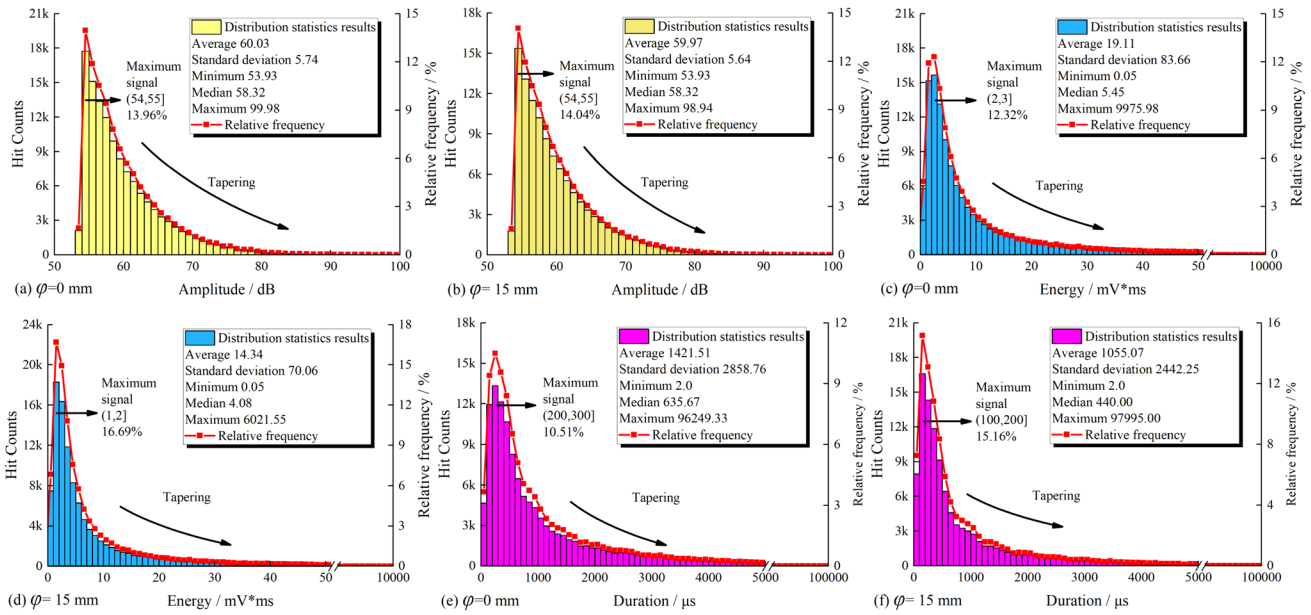


**Fig. 18** Distribution and statistical results of amplitude, energy and duration of AE signal: **a, c** and **e**  $\varphi=0$  mm specimen and **b, d** and **f**  $\varphi=15$  mm specimen

which is 16.69%, and the higher the energy, the smaller the proportion. The mean value of the hit signal energy is 14.34 mV\*ms, and the standard deviation is 70.06 mV\*ms. The comparison shows that the energy distribution of the hit signal varies significantly.

As can be seen from Fig. 18e, for the  $\varphi=0$  mm specimen, the largest proportion of the hit signal duration is in the interval (200,300)  $\mu$ s (10.51%), and the longer the duration, the smaller the proportion. The mean value of the hit signal duration is 1421.51  $\mu$ s, and the standard deviation is 2858.76  $\mu$ s. Fig. 18f shows that for the  $\varphi=15$  mm specimen, the largest proportion of the hit signal duration is in the interval (100,200)  $\mu$ s, which is 15.16%, and the proportion decreases with higher duration. The mean value of the hit signal duration is 1055.07  $\mu$ s, with a standard deviation of 2442.25  $\mu$ s. The variability of the hit signal duration

distribution is evident from the comparison. For the specimen with  $\varphi=15$  mm, the high-frequency signal increased in the hit signal because the local source energy was released in the form of short-term high-frequency tensile longitudinal fluctuations during material splitting, collapsing and spalling, which led to a change in the duration of the hit signal distribution from (200,300)  $\mu$ s to (100,200)  $\mu$ s. This also reduces the standard deviation of the durations, making the overall dispersion of the hit signal durations less discrete and more concentrated towards lower duration signals.

**Correlation characteristics of AE parameters**

The correlation between different parameters of the AE waveform is an important indicator to evaluate the correlation characteristics of AE parameters. Figures. 19 and 20

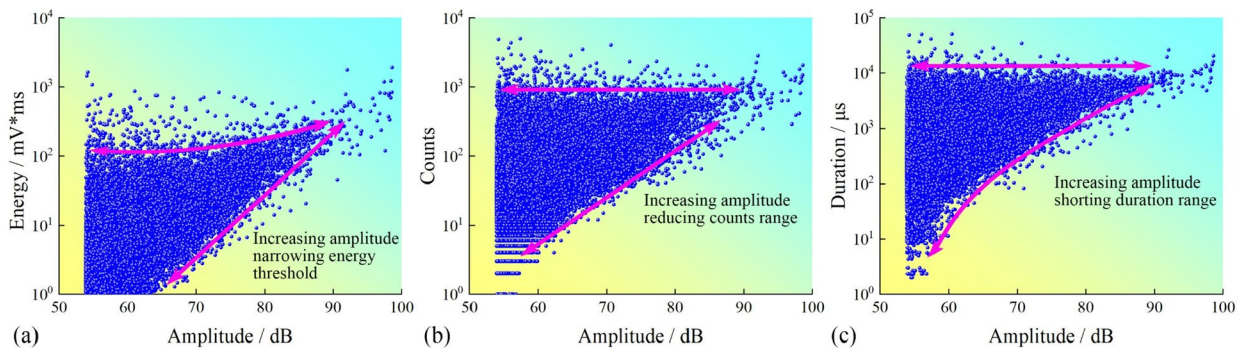


**Fig. 19** Diagram of the correlation between energy-amplitude, count-amplitude and duration-amplitude of AE signal for  $\varphi=0$  mm specimen



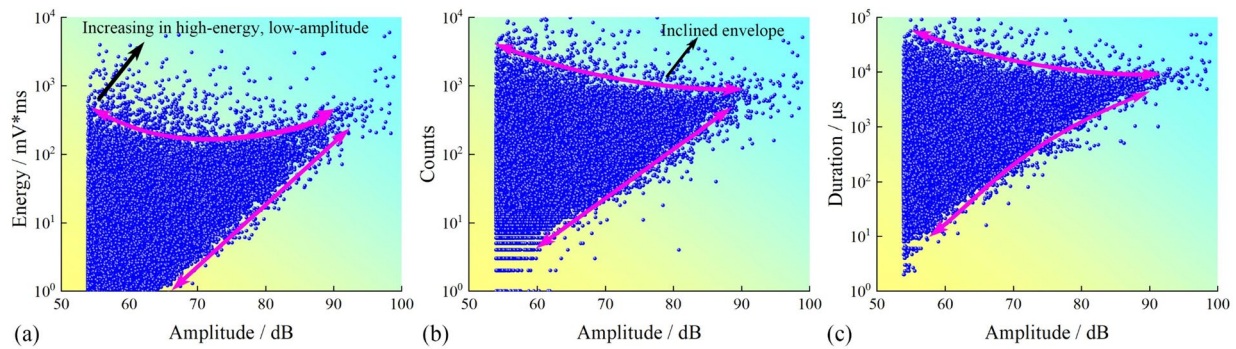


**Fig. 20** Diagram of the correlation between energy-amplitude, count-amplitude and duration-amplitude of AE signal for  $\varphi = 15$  mm specimen

show the correlations between the energy-amplitude, counts-amplitude and duration-amplitude of AE for  $\varphi = 0$  mm and  $\varphi = 15$  mm specimens, respectively.

For the  $\varphi = 0$  mm specimen, it can be seen from Fig. 19a that the energy-amplitude correlation of the hit signal forms a linearly inclined purple dividing line at the lower edge of the energy threshold and a slightly curved downward purple dividing line at the upper edge of the energy threshold as the amplitude varies from low to high. As the amplitude gradually increases, the difference in energy levels decreases and remains essentially at the same magnitude. As can be seen from Fig. 19b, in the counts-amplitude correlation of the hit signal, as the amplitude varies from low to high, the lower edge of the count range forms a linearly sloping purple dividing line, and the upper edge of the count range, an essentially flat purple dividing line. As the amplitude gradually increases, the count range gradually decreases, remaining essentially at the same magnitude. As can be seen from Fig. 19c, the duration-amplitude correlation for the hit signal forms a curved purple dividing line at the right edge of the amplitude, the lower edge of the duration and the upper edge of the duration, forming an essentially flat purple dividing line. As the magnitude gradually increases, the difference in duration becomes smaller and remains at the same magnitude.

The correlation diagram for the  $\varphi = 15$  mm specimen is shown in Fig. 20. Comparing Fig. 19, it can be seen that for the AE parameter correlations, the main differences are concentrated in the low-amplitude signal region, with more signals carrying high energy in the low-amplitude signal, more signals with high orders of magnitude of AE counts in the low-amplitude signal and more signals with longer durations in the low-amplitude signal. Combined with the failure results of the specimen in Fig. 9, this may be due to the presence of circular weak filling, which makes the planar weak filling and circular weak filling synergistically bear the load, mitigating the sudden and violent release of deformation energy, prolonging the shear main crack initiation and propagation time and prolonging the fluctuation time of

the elastic wave when the local source energy of the material is released as a shear wave, resulting in low amplitude-high energy, low amplitude-high magnitude counts and low amplitude-long duration of the hit signal increases.

### Characteristics of the spatiotemporal distribution of microfracture events

The spatiotemporal evolution and distribution characteristics of internal microfracture events during the damage of the specimen are analysed using AE 3D spatial localization technique. The essence of acoustic source localisation is the process of solving for the time of generation of the source and its corresponding location (Shen 2015). In combination with the previous analysis,  $\varphi = 0$  mm and  $\varphi = 15$  mm specimens were selected as representatives, and the results of the AE monitoring system for locating the microfracture events during the loading of the specimens are shown in Figs. 21 and 22.

In Fig. 21, at  $t = 200$  s, the microfracture events are concentrated near the upper and lower ends of the specimen. At  $t = 400$  s, the microfracture events accumulate at the left and right ends of the planar weak filling, which means that the left and right ends of the planar weak filling act as a stress concentration region, where local material failure and microfracture initiation will occur first. As the loading continues, at  $t = 500$  s, a large accumulation of microcracking events can be observed in the planar weak filling area. At the left end of the planar weak filling, the microfracture events start to spread around, with the main direction being upwards and downwards. At the right end of the planar weak filling, the microfracture events spread upwards and downwards. This means that microcrack initiation and propagation occur in the left end and right end of the planar weak filling and that the microcracks converge to nucleate as they continue to load, manifesting as an accumulation of microfracture events nucleating. At  $t = 640$  s, the specimen reaches its peak stress and is about to be destabilised, with microfracture events

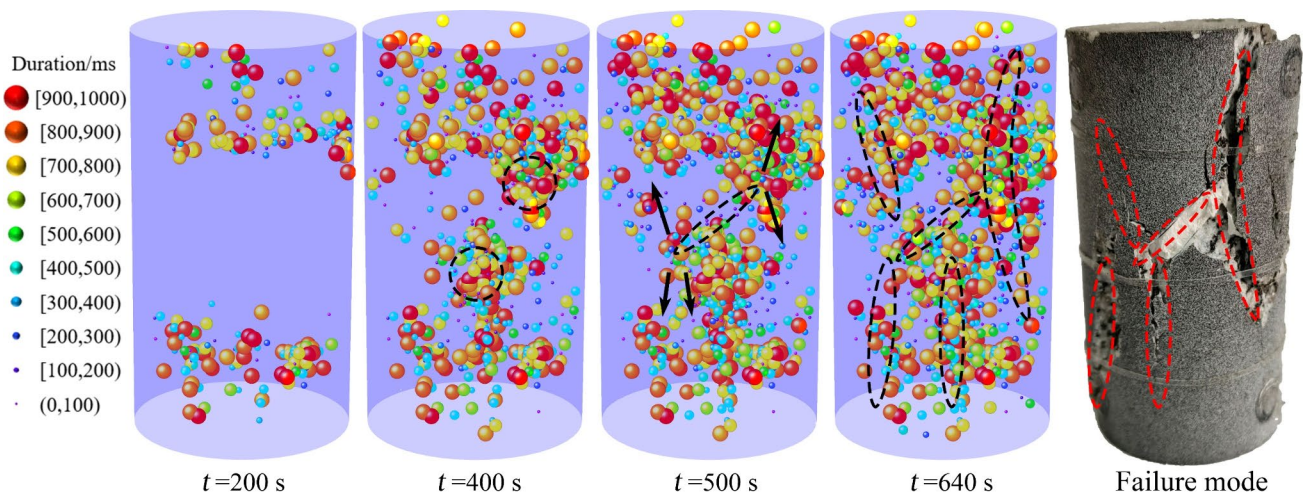


**Fig. 21** Spatial evolution of microfracture events and distribution characteristics of  $\varphi=0$  mm specimen

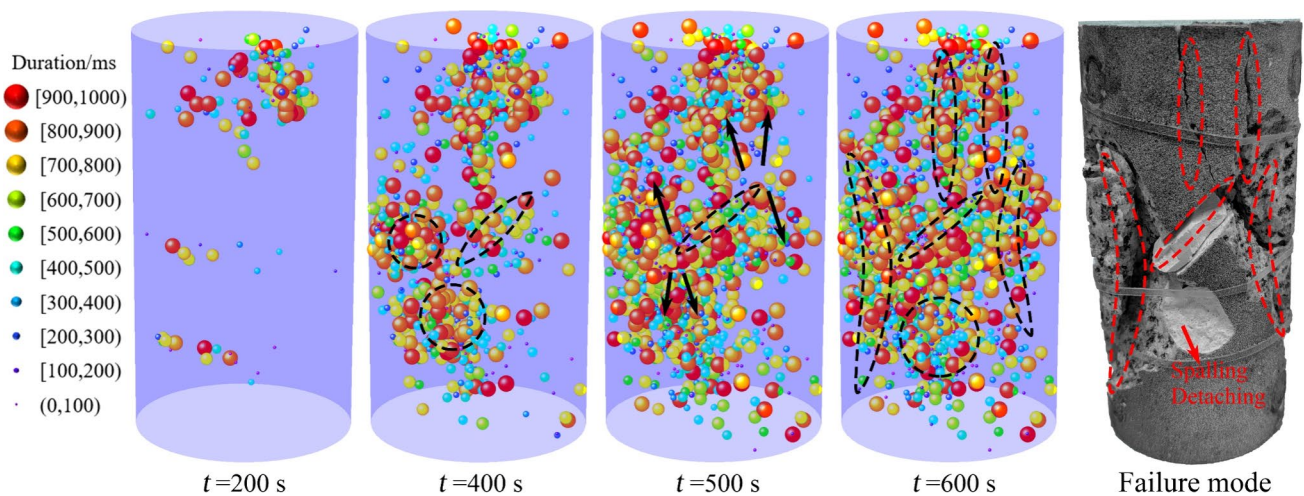


**Fig. 22** Spatial evolution of microfracture events and distribution characteristics of  $\varphi=15$  mm specimen

accumulating and nucleating in the planar weak filling and surrounding bedrock. The nucleation area above and below the left end of the planar weakly filled is distributed in a “spindle” pattern. At the right end of the planar weak filling, the nucleation of the microfracture event resembles a “crescent” pattern. This is shown in the black dashed box in the figure. The spatial distribution of the main fracture surface is distributed in the weakly filled area, above the left end, below the bedrock and at the right end of the bedrock, as shown by the red dashed box in Fig. 21.

As can be seen in Fig. 22, there is some variability in the evolution of micro-fracture events in the presence of circular weak filling. It is mainly manifested in the late loading stage, the microfracture events inside the specimen accumulate and nucleate at the planar and circular weak filling. At the same time, the left bedrock at the left end of the planar weak filling and the right bedrock at the right end were distributed

in a similar “crescent” pattern, which, when combined with the specimen failure results, showed a serious collapsing in this area. This is because when the circular weak filling exists, the planar weak filling and the circular weak filling cooperate to bear the load, the effective bearing capacity of the bedrock on both sides of the circular weak filling decreases, and when the rock body is destabilised, the main cracks originated from the left end and right end of the planar weak filling expand at the bedrock, resulting in the convergence of micro-cracks, the propagation space becomes smaller, and the macroscopic formation of lamellae. In the bedrock above the right end of the planar weak filling, the microfracture events accumulate and nucleate, and the main fracture extends in this region when the specimen is destabilised and damaged.

Combined with the above spatiotemporal evolution and distribution of microfracture events, it is clear that the

weakly filled area will first become the area of microfracture event accumulation and gradually spread. The presence of circular weak filling causes the formation of bedrock gneisses, leading to the nucleation of bedrock microfracture events at the corresponding locations on both sides. The nucleation of microfracture events in the bedrock area is the result of the formation of the main fracture surface. The accumulation and distribution characteristics of microfracture events in the weak filling areas and bedrock areas can be used as an indicator to predict the destabilisation of rock masses and to evaluate the propensity, severity and timing of destabilisation of rock masses containing the weak filling.

## Discussion

From the analysis of the above results, it can be seen that the influence of the presence of weak filling on the mechanical behaviour and AE parameter characteristics of the rock mass is significant. The changes in the mechanical behaviour indicate that the presence of weak filling leads to the differentiation of the surface deformation evolution pattern and the final failure mode when the rock mass is subjected to loads. This is due to the fact that the presence of weak filling affects the load transfer path when the rock mass is subjected to forces. When the bedrock is loaded in concert with the weak filling, it is inevitably different from the intact rock mass; therefore, the change in the mechanical behaviour of the weakly filled rock mass is certain. The surface deformation behaviour is the apparent manifestation of the mechanical characteristics of the rock mass during loading, and the variability of the failure mode is the final result of the change in the mechanical characteristics of the rock mass.

The results of the analyses concerning the characteristics of the AE parameters show that the presence of weak filling leads to changes in the acoustic properties of the rock mass. In general, the change in acoustic characteristics indicates a change in the way the elastic energy is released and distributed during the initiation and propagation of microcracks in the rock mass, and therefore, the distribution and correlation characteristics of the AE parameters change as a result. The changes in the characteristics of the AE parameters are the acoustic manifestation of the changes in the mechanical behaviour, which is the acoustic evidence of the changes in the physical and mechanical properties of the apparent rock mass.

The interconnection between the mechanical behaviour of the rock mass and the characteristics of the AE parameters should be viewed in a dialectical and unified way. For example, the final failure mode of specimens with different distribution of weak fill changes accordingly. This suggests that when facing the stability control of weakly filled rock masses, we should focus on the possibility of large

deformation in weakly filled areas with different geometrical characteristics of the rock masses and the tendency of final failure. Combined with the spatial and temporal evolution and distribution of microfracture events, it can be seen that the weakly filled areas will first become the accumulation areas of microfracture events, and gradually spread. The accumulation and distribution of microfracture events in weakly filled areas and bedrock can be used as an indicator to predict the destabilisation of the rock masses and to evaluate the destabilisation tendency, severity and timeliness of the weakly filled rock masses. It is due to the change of the mechanical behaviour of the rock mass that the final destabilisation of the rock mass is bound to have a certain degree of variability and severity. At the same time, the analysis of AE parameters is both an acoustic characterisation of this change in mechanical behaviour and a positive way to address the consequences of this change in mechanical behaviour. For example, the use of AE spatial microfracture event localisation may be useful for monitoring, and predicting, the location of spatial gestation of rock mass instability.

## Conclusions

In this paper, uniaxial compression experiments were carried out on granite with simultaneous planar weak filling and circular weak filling of different diameters. The experiments were carried out with the aid of both 3D DIC and AE monitoring system. The mechanical behaviour and acoustic characteristics of the specimens were analysed. In addition, the spatial distribution characteristics of microfracture events within the specimens were analysed using AE spatial localisation technique, and the results show that AE technique has excellent ability in the research on the spatial fracture characteristics of rock masses containing weak filling. The main conclusions are as follows:

- (1) The contact area between the planar weak filling and bedrock is in a state of severe local deformation, extending towards the bedrock at both ends, and the main fracture extends in this area when the specimen is destabilised. The annular region of the contact between the circular weak filling and the bedrock is in a severe deformation area, where detaching from the bedrock and spalling behaviour occurs. The specimen is damaged as a whole shear failure, and the presence of circular weak filling has a certain guiding effect on the propagation of secondary cracks.
- (2) The presence of planar and circular weak filling leads to increased fluctuation of AE. The AE hit signal is dominated by the shear signal, but the presence of circular weak filling increases the splitting signal component.



- (3) The AE signal is dominated by low-amplitude signals. In the presence of circular weak filling, the most dominant signal has a lower energy interval and a shorter duration. The difference in the correlation of AE parameters is concentrated in the low-amplitude signal region, which is reflected in the increase of signals carrying high energy in the low-amplitude signal, the increase of signals with high orders of magnitude and the increase of signals with long duration.
- (4) Weakly filled areas will first become areas of spatiotemporal accumulation of microfracture events and will gradually spread. The accumulation of microfracture nucleation in bedrock areas is caused by the formation of the main fracture surface. The accumulation and distribution characteristics of microfracture events in the weak filling areas and bedrock can be used as indicators to predict the destabilisation of rock masses and to evaluate the propensity, severity and timing of destabilisation of rock masses containing the weak filling.

**Funding** The work was financially supported by the National Key Research and Development Program of China (No. 2021YFB3401501) and the Central University Basic Research Fund of China (2022JCCXLJ01).

**Data availability** The data are available from the corresponding author on reasonable request.

## Declarations

**Competing interests** The authors declare no competing interests.

## References

- Aggelis DG, Mpalaskas AC, Matikas TE (2013) Acoustic signature of different fracture modes in marble and cementitious materials under flexural load. *Mech Res Commun* 47:39–43. <https://doi.org/10.1016/j.mechrescom.2012.11.007>
- Ai T, Zhang R, Zhou HW, Pei JL (2014) Box-counting methods to directly estimate the fractal dimension of a rock surface. *Appl Surf Sci* 314:610–621. <https://doi.org/10.1016/j.apsusc.2014.06.152>
- Asadzadeh M, Hossaini MF, Moosavi M, Masoumi H, Ranjith PG (2019) Mechanical characterisation of jointed rock-like material with non-persistent rough joints subjected to uniaxial compression. *Eng Geol* 260:105224. <https://doi.org/10.1016/j.enggeo.2019.105224>
- Brown ET (1981) Rock characterization, testing & monitoring: ISRM suggested methods. Pergamon Press, London, UK
- Carpinteri A, Chiaia B, Invernizzi S (1999) Three-dimensional fractal analysis of concrete fracture at the meso-level. *Theor Appl Fract Mech* 31:163–172. [https://doi.org/10.1016/S0167-8442\(99\)00011-7](https://doi.org/10.1016/S0167-8442(99)00011-7)
- Chai SB, Wang H, Yu LY, Shi JH, Abi E (2020) Experimental study on static and dynamic compression mechanical properties of filled rock joints. *Latin Am J Solids Struct* 17(3):e264. <https://doi.org/10.1590/1679-78255988>
- Chai SB, Jia YS, Du YX, Hu B, Li XP (2022) Experimental study on compression mechanical characteristics of filled rock joints after multiple pre-impacts. *Sci Rep-Uk* 12(1):13628. <https://doi.org/10.1038/s41598-022-15849-5>
- Chajed S, Singh A (2024) Acoustic emission (ae) based damage quantification and its relation with ae-based micromechanical coupled damage plasticity model for intact rocks. *Rock Mech Rock Eng*. 10.1007/s00603-023-03686-5
- Chen GQ, Li TB, Zhang GF, Yin HY, Zhang H (2014) Temperature effect of rock burst for hard rock in deep-buried tunnel. *Nat Hazards* 72(2):915–926. <https://doi.org/10.1007/s11069-014-1042-6>
- Chen GQ, Li H, Wei T, Zhu J (2021) Searching for multistage sliding surfaces based on the discontinuous dynamic strength reduction method. *Eng Geol* 286:106086. <https://doi.org/10.1016/j.enggeo.2021.106086>
- Ding SX, Jing HW, Chen KF, Xu GA, Meng B (2017) Stress evolution and support mechanism of a bolt anchored in a rock mass with a weak interlayer. *Int J Min Sci Technol* 27:573–580. <https://doi.org/10.1016/j.ijmst.2017.03.024>
- Dong YL, Pan B (2017) A review of speckle pattern fabrication and assessment for digital image correlation. *Exp Mech* 57(8):1161–1181. <https://doi.org/10.1007/s11340-017-0283-1>
- Han ZY, Xie SJ, Li DY, Zhu QQ, Yan ZW (2022) Dynamic mechanical behavior of rocks containing double elliptical inclusions at various inclination angles. *Theor Appl Fract Mech* 121:103544. <https://doi.org/10.1016/j.tafmec.2022.103544>
- Huang CC, Yang WD, Duan K, Fang LD, Wang L, Bo CJ (2019) Mechanical behaviors of the brittle rock-like specimens with multi-non-persistent joints under uniaxial compression. *Constr Build Mater* 220:426–443. <https://doi.org/10.1016/j.conbuildmat.2019.05.159>
- Ishida T, Labuz JF, Manthei G, Meredith PG, Nasser MHB, Shin K, Yokoyama T, Zang A (2017) ISRM suggested method for laboratory acoustic emission monitoring. *Rock Mech Rock Eng* 50(3):665–674. <https://doi.org/10.1007/s00603-016-1165-z>
- Jahanian H, Sadaghiani MH (2015) Experimental study on the shear strength of sandy clay infilled regular rough rock joints. *Rock Mech Rock Eng* 48(3):907–922. <https://doi.org/10.1007/s00603-014-0643-4>
- Janeiro RP, Einstein HH (2010) Experimental study of the cracking behavior of specimens containing inclusions (under uniaxial compression). *Int J Fract* 164:83–102. <https://doi.org/10.1007/s10704-010-9457-x>
- Kendall RS (2017) The old red sandstone of Britain and Ireland—a review. *Proc Geol Assoc* 128(3):409–421. <https://doi.org/10.1016/j.pgeola.2017.05.002>
- Li HQ, Wong LNY (2012) Influence of flaw inclination angle and loading condition on crack initiation and propagation. *Int J Solids Struct* 49:2482–2499. <https://doi.org/10.1016/j.ijsolstr.2012.05.012>
- Li LR, Deng JH, Zheng L, Liu JF (2017) Dominant frequency characteristics of acoustic emissions in white marble during direct tensile tests. *Rock Mech Rock Eng* 50:1337–1346. <https://doi.org/10.1007/s00603-016-1162-2>
- Li DY, Gao FH, Han ZY, Zhu QQ (2020) Experimental evaluation on rock failure mechanism with combined flaws in a connected geometry under coupled static-dynamic loads. *Soil Dyn Earthq Eng* 132:106088. <https://doi.org/10.1016/j.soildyn.2020.106088>
- Li S, Lin H, Hu SB (2023) Mechanical behavior of anchored rock with an infilled joint under uniaxial loading revealed by AE and DIC monitoring. *Theor Appl Fract Mech* 123:103709. <https://doi.org/10.1016/j.tafmec.2022.103709>
- Liu XL, Liu Z, Li XB, Gong FQ, Du K (2020) Experimental study on the effect of strain rate on rock acoustic emission characteristics. *Int J Rock Mech Min Sci* 133:104420. <https://doi.org/10.1016/j.ijrmms.2020.104420>
- Liu HX, Jin HW, Yuan Y, Yin Q, Guzev MA, Turbakov MS (2023) Experimental study on mechanical and fracture characteristics of inclined weak-filled rough joint rock-like specimens. *Theor Appl Fract Mech* 126:103950. <https://doi.org/10.1016/j.tafmec.2023.103950>
- Liu XW, Deng W, Liu B, Liu QS, Zhu YG, Fan Y (2023) Influence analysis on the shear behaviour and failure mode of grout-filled jointed rock using 3D DEM coupled with the cohesive zone model. *Comput Geotech* 155:105165. <https://doi.org/10.1016/j.compgeo.2022.105165>
- Luo XY, Cao P, Lin QB, Li S (2021) Mechanical behaviour of fracture-filled rock-like specimens under compression-shear loads:

- An experimental and numerical study. *Theor Appl Fract Mech* 113:102935. <https://doi.org/10.1016/j.tafmec.2021.102935>
- Luo XY, Cao P, Liu TY, Zhao QX, Meng G, Fan Z, Xie WP (2022) Mechanical behaviour of anchored rock containing weak interlayer under uniaxial compression: laboratory test and coupled DEM-FEM simulation. *Minerals* 12(4):492. <https://doi.org/10.3390/min12040492>
- Ma D, Duan H, Liu J, Li X, Zhou Z (2019) The role of gangue on the mitigation of mining-induced hazards and environmental pollution: an experimental investigation. *Sci Total Environ* 664:436–448. <https://doi.org/10.1016/j.scitotenv.2019.02.059>
- Miao ST, Pan PZ, Wu ZH, Li SJ, Zhao SK (2018) Fracture analysis of sandstone with a single filled flaw under uniaxial compression. *Eng Fract Mech* 204:319–343. <https://doi.org/10.1016/j.engfracmech.2018.10.009>
- Munoz H, Taheri A, Chanda EK (2016) Pre-peak and post-peak rock strain characteristics during uniaxial compression by 3D digital image correlation. *Rock Mech Rock Eng* 49(7):2541–2554. <https://doi.org/10.1007/s00603-016-0935-y>
- Naghadehi MZ (2015) Laboratory study of the shear behaviour of natural rough rock joints infilled by different soils. *Period Polytech Civil Eng* 59(3):413–421. <https://doi.org/10.3311/PPci.7928>
- Nasseri MHB, Tatone BSA, Grasselli G, Young RP (2009) Fracture toughness and fracture roughness interrelationship in thermally treated westerly granite. *Pure Appl Geophys* 166:801–822. <https://doi.org/10.1007/s00024-009-0476-3>
- Niu Y, Zhou XP, Zhou LS (2020) Fracture damage prediction in fissured red sandstone under uniaxial compression: acoustic emission b-value analysis. *Fatigue Fract Eng Mater Struct* 43(1):175–190. <https://doi.org/10.1111/ffe.13113>
- Pan PZ, Miao ST, Jiang Q, Wu ZH, Shao CY (2019) The influence of infilling conditions on flaw surface relative displacement induced cracking behavior in hard rock. *Rock Mech Rock Eng* 53(10):4449–4470. <https://doi.org/10.1007/s00603-019-02033-x>
- Sharafisafa M, Shen LM, Zheng YG, Xiao JZ (2019) The effect of flaw filling material on the compressive behaviour of 3D printed rock-like discs. *Int J Rock Mech Min Sci* 117:105–117. <https://doi.org/10.1016/j.ijrmms.2019.03.031>
- Shen GT (2015) Acoustic emission detection technology and application. Science Press, Beijing, China
- Shimbo T, Shinzo C, Uchii U, Itto R, Fukumoto Y (2022) Effect of water contents and initial crack lengths on mechanical properties and failure modes of pre-cracked compacted clay under uniaxial compression. *Eng Geol* 301:106593. <https://doi.org/10.1016/j.enggeo.2022.106593>
- Song H, Zhang H, Fu D, Kang Y, Huang G, Qu C, Cai Z (2013) Experimental study on damage evolution of rock under uniform and concentrated loading conditions using digital image correlation. *Fatigue Fract Eng Mater Struct* 36(8):760–768. <https://doi.org/10.1111/ffe.12043>
- Srivastava LP, Singh M (2015) Empirical estimation of strength of jointed rocks traversed by rock bolts based on experimental observation. *Eng Geol* 197:103–111. <https://doi.org/10.1016/j.enggeo.2015.08.004>
- Su QQ, Ma QY, Ma DD, Yuan P (2021) Dynamic mechanical characteristic and fracture evolution mechanism of deep roadway sandstone containing weakly filled joints with various angles. *Int J Rock Mech Min Sci* 137:104552. <https://doi.org/10.1016/j.ijrmms.2020.104552>
- Sutton MA, Orteu JJ, Schreier HW (2009) Image correlation for shape, motion and deformation measurements. Springer USA 5:81–88
- Tang Y, Zhang HL, Guo XX, Ren T (2022) Literature survey and application of a full-field 3D-DIC technique to determine the damage characteristic of rock under triaxial compression. *Int J Damage Mech* 31(7):1082–1095. <https://doi.org/10.1177/10567895221089660>
- Tian YC, Liu QS, Ma H, Liu Q, Deng PH (2018) New peak shear strength model for cement filled rock joints. *Eng Geol* 233:269–280. <https://doi.org/10.1016/j.enggeo.2017.12.021>
- Wang HC, Zhao J, Li J, Wang HJ, Braithwaite CH, Zhang QB (2022) Fracturing and AE characteristics of matrix-inclusion rock types under dynamic Brazilian testing. *Int J Rock Mech Min Sci* 157:105164. <https://doi.org/10.1016/j.ijrmms.2022.105164>
- Yin TB, Li Q, Li XB (2019) Experimental investigation on mode I fracture characteristics of granite after cyclic heating and cooling treatments. *Eng Fract Mech* 222:106740. <https://doi.org/10.1016/j.engfracmech.2019.106740>
- Yin TB, Yin JW, Wu Y, Yang Z, Liu XL, Zhuang DD (2022) Water saturation effects on the mechanical characteristics and fracture evolution of sandstone containing pre-existing flaws. *Theor Appl Fract Mech* 122:103605. <https://doi.org/10.1016/j.tafmec.2022.103605>
- Yu J, Chen X, Cai YY, Li H (2016) Triaxial test research on mechanical properties and permeability of sandstone with a single joint filled with gypsum. *KSCE J Civ Eng* 20(6):2243–2252. <https://doi.org/10.1007/s12205-015-1663-7>
- Yu ML, Zuo JP, Sun YJ, Mi CN, Li ZD (2022) Investigation on fracture models and ground pressure distribution of thick hard rock strata including weak interlayer. *Int J Min Sci Technol* 32(1):137–153. <https://doi.org/10.1016/j.ijmst.2021.10.009>
- Zhang QB, Zhao J (2013) Effect of loading rate on fracture toughness and failure micromechanisms in marble. *Eng Fract Mech* 102:288–309. <https://doi.org/10.1016/j.engfracmech.2013.02.009>
- Zhang R, Dai F, Gao MZ, Xu NW, Zhang CP (2015) Fractal analysis of acoustic emission during uniaxial and triaxial loading of rock. *Int J Rock Mech Min Sci* 79:241–249. <https://doi.org/10.1016/j.ijrmms.2015.08.020>
- Zhang J, Peng WH, Liu FY, Zhang HX, Li ZJ (2016) Monitoring rock failure processes using the Hilbert-Huang transform of acoustic emission signals. *Rock Mech Rock Eng* 49(2):427–442. <https://doi.org/10.1007/s00603-015-0755-5>
- Zhang ZH, Deng JH, Zhu JB, Li LR (2018) An experimental investigation of the failure mechanisms of jointed and intact marble under compression based on quantitative analysis of acoustic emission waveforms. *Rock Mech Rock Eng* 51(7):2299–2307. <https://doi.org/10.1007/s00603-018-1484-3>
- Zhang YC, Jiang YJ, Asahina D, Wang CS (2020) Experimental and numerical investigation on shear failure behavior of rock-like samples containing multiple non-persistent joints. *Rock Mech Rock Eng* 53(10):4717–4744. <https://doi.org/10.1007/s00603-020-02186-0>
- Zhou HW, Xie H (2008) Direct estimation of the fractal dimensions of a fracture surface of rock. *Surf Rev Lett* 10:751–762. <https://doi.org/10.1142/S0218625X03005591>
- Zhu QQ, Li DY, Han ZY, Li XB, Zhou ZL (2019) Mechanical properties and fracture evolution of sandstone specimens containing different inclusions under uniaxial compression. *Int J Rock Mech Min Sci* 115:33–47. <https://doi.org/10.1016/j.ijrmms.2019.01.010>
- Zhu X, Fan J, He CL, Tang Y (2022) Identification of crack initiation and damage thresholds in sandstone using 3D digital image correlation. *Theor Appl Fract Mech* 122:103653. <https://doi.org/10.1016/j.tafmec.2022.103653>
- Zhuang XY, Chun JW, Zhu HH (2014) A comparative study on unfilled and filled crack propagation for rock-like brittle material. *Theor Appl Fract Mech* 72:110–120. <https://doi.org/10.1016/j.tafmec.2014.04.004>